THE ASTRONOMICAL JOURNAL VOLUME 104, NUMBER 6 DECEMBER 1992

THE NEARBY 2 $\mathcal{M}_\odot$ BOK GLOBULE LBN 11: SUB-SONIC MOLECULAR CLUMPS IN A MAGNETIC ENVIRONMENT

DAN P. CLEMENS
Astronomy Department, Boston University, 725 Commonwealth Avenue, Boston, Massachusetts 02215

ROBERT L. DICKMAN,[1]
Five College Radio Astronomy Observatory, 619 I Lederle Graduate Research Center, University of Massachusetts, Amherst, Massachusetts 01003

DAVID R. CIARDI[2]
Astronomy Department, Boston University, 725 Commonwealth Avenue, Boston, Massachusetts 02215

Received 5 June 1992; revised 22 July 1992

ABSTRACT

We have mapped the nearby small Bok globule LBN 11 (size $\sim$0.3 pc, distance $\sim$110 pc) in the millimeter lines of CO at very high dispersion (65 m s^{-1} per channel), obtained co-added *IRAS* survey images of the cloud, and measured the optical linear polarization of sixteen stars close to the cloud center. The molecular lines and *IRAS* images reveal a low mass cloud ($\sim 2\ \mathcal{M}_\odot$) with a moderately dense core ($\bar{n} \leqslant 10^{4.5}$ cm^{-3}) which has not formed stars. The high spectral resolution CO lines reveal the presence of several individual kinematic and spatial components ("clumps") within the cloud, which exhibit subsonic linewidths. Such distinct clumping in so small a cloud has not previously been seen. CS and SO maps of the ^{13}CO core region made at 25″ resolution confirm the presence of the dense gas expected from the radial density distribution inferred from the ^{13}CO observations. Overall, the cloud is in a state of rotation, with a rotation rate of 3.6 ± 1.0 km s^{-1} pc^{-1}, for the region strongest in ^{13}CO emission. The rotation direction, determined from a solid body fit to the CO isotopic lines, lies along P.A. $= -86 \pm 11°$. This is parallel to the long axis of the cloud, as well as nearly parallel to the direction of the embedded magnetic field traced by the optical polarizations measured for the 16 stars, P.A. $= 81.6 \pm 0.5°$. The dispersion of the projected magnetic field direction is quite small ($\sim 6°$), but is shown to be largest for characteristic spatial separations of 0.1–0.2 pc between pairs of stars. The distributions of CO and ^{13}CO clump sizes also peak near 0.15 pc, suggesting a possible connection between the magnetic field and the clumpy state of the cloud. The ^{13}CO clumps may arise from fragmentation of the rapidly rotating core and could signify the presence of a very young protobinary. The CO clumps are transitory and may be due to Alfvén waves driven into the cloud periphery.

1. INTRODUCTION

How does the presence of a magnetic field and rotation affect the formation of young stars inside a cloud core? In order to investigate this question, we have probed the very nearby cloud LBN 11 (Lynds 1965), which also appears as entry 63 in the list of small molecular clouds compiled by Clemens & Barvainis (1988, hereafter CB). The distance to this cloud is about 110 pc, based on its positional and radial velocity association with the L 134 region, whose distance was estimated via a reddening-distance relation by Franco (1989). The optically opaque core of LBN 11 has an angular size of about 7×11 arcmin, corresponding to a physical size of about 0.3 pc for the cloud, placing it near the mean size of the small Bok globules surveyed for CO and *IRAS* emission by Clemens *et al.* (1991; hereafter CYH).

Several previous studies of globule magnetic fields have yielded interesting results. Jones *et al.* (1984) used near-IR techniques to build a detailed map of the magnetic field associated with the large Bok globule Coalsack 2, and contended that quasistatic collapse of the cloud could explain the ordering of the field lines for that cloud. Joshi *et al.* (1985) and Williams *et al.* (1985) studied the large globules B 5 and B 361, respectively. Vrba *et al.* (1986) studied the magnetic field directions associated with the star forming globule B 335, finding a magnetic field which is parallel to both the ambient medium and to the high velocity outflow mapped by Goldsmith *et al.* (1984). However, Hodapp (1987) probed the polarizations of stars much closer to the opaque core of B 335 and found that the magnetic field was more disordered than that found by Vrba *et al.* Klebe & Jones (1990) used background starlight to probe the density distributions and polarization characteristics of three Bok globules. Of their three, B 118 has the smallest size ($\sim$0.2 pc—similar to that of LBN 11) and shows polarization vectors which are generally aligned. Klebe and Jones argue that globules this small are those with maximum ambipolar diffusion rates in the molecular material (Myers & Goodman 1988). Under those conditions, the once-embedded magnetic fields should exist

[1]Also Division of Astronomical Sciences, National Science Foundation.
[2]Currently Department of Physics and Astronomy, University of Wyoming.

 0004-6256/92/122165-24$00.90

mostly in the peripheries of these clouds, leading to apparently uniform polarization patterns.

The "standard picture" of the formation of a dense molecular cloud from a diffuse collection of magnetized gas and dust involves quasistatic contraction of the material along the magnetic field lines, with much less contraction along directions perpendicular to the field lines (Mouschovais 1976a,b). This collapse should preferentially generate clouds with oblate or pancake shapes, with their magnetic fields directed parallel to their minor axes. Several large dark cloud complexes do show the expected morphologies and polarization orientations (e.g., L 204: McCutcheon *et al.* 1986; the Taurus dark clouds: Heyer *et al.* 1987). However, there are also configurations which do not fit the standard picture (e.g., ρ Oph: Vrba *et al.* 1976).

It is not clear how Bok globules should fit into the standard picture, since their formation is not generally thought to proceed along quiescent pathways (Schneps *et al.* 1980; Zealey *et al.* 1983; Dickman & Clemens 1983; Leung 1985; Kimura & Tosa 1991). Hodapp (1987) has proposed a scenario in which ram pressure due to the diffuse intercloud medium strips cloud envelopes. In this picture, the intrinsic magnetic field lines of a globule are stretched from the core to the displaced envelope, leading to polarizations which trace out the stretched field lines.

In order to begin to address the relationship between embedded magnetic fields and star formation, we have conducted a detailed study of the very nearby small Bok globule LBN 11. The goals of the study are to characterize the magnetic, star formation, structural, and kinematic states of the cloud. By exploring possible links between these physical properties, we seek to ascertain the relative importance of the magnetic field, cloud rotation, fragmentation, and environment in ordering the structure and stability of this seemingly simple cloud.

We use observations of the optical polarization of stars lying behind LBN 11 to probe the magnetic field direction. High spectral resolution CO and HCO^+ isotopic mapping and high angular resolution CS and SO mapping are used to establish the kinematics and structure of the globule gas. Co-added *IRAS* survey imaging is used to both search for embedded and associated young stellar objects and to delineate the structure of the extended dust component of the cloud.

These data paint a picture of a quiescent but highly clumpy, rotating globule. A well-delineated dense core is present, surrounded by a region of exceedingly uniform magnetic field lines. Interestingly, the magnetic field exhibits a characteristic directional length scale which is nearly identical to the sizes of the gas clumps, implying that the field and the clumps may be coupled physically. No embedded stars are detectable in LBN 11.

In the data section of this paper, we present basic data concerning LBN 11 including distance estimates. We also present our optical polarization measurements and compare the direction of the cloud magnetic field to that of the Galactic field. The characteristic magnetic field length scale in our data is introduced here. The millimeter observations are presented as a series of maps of integrated line emission and sample line profiles. The *IRAS* data are presented and examined for the presence of embedded point sources and extended emission.

The discussion section of this paper contains several detailed examinations of the physical properties of LBN 11. The overall density structure and cloud mass are established in Sec. *3.1*. Chemical abundances and spatial variations of those abundances are pursued in Sec. *3.2*. A direct, simple measurement of the rotational state of the globule gas is performed in Sec. *3.3*.

Section *3.4* contains a detailed analysis of the information contained in the molecular line profiles. Two regions of the cloud are found to exhibit CO self-absorptions, as described in Sec. *3.4.2*. Because the presence of multiple gas components is strongly suggested by the spectral line shapes, detailed profile fitting was performed, as described in Sec. *3.4.3*. The results of this process establish the subsonic nature of the gas components (Sec. *3.4.4*). Because the profile fitting establishes highly precise radial velocities for the gas, the rotational state of the cloud is reexamined in Sec. *3.4.5*. A rotation curve indicating differential rotation is found; we suggest it may indicate the presence of a protobinary in the cloud core. Finally, the cloud molecular line profiles are analyzed using channel maps, leading to a catalog of CO and ^{13}CO clumps (Sec. *3.4.6*).

The nature of the gas clumps, and their possible relation to the magnetic field are explored in Sec. *3.5*. As discussed in Sec. *3.6*, the CS and SO features and structure of the core suggest that future star formation is possible in LBN 11. A detailed summary of our findings is contained in Sec. 4.

2. DATA

2.1 LBN 11

LBN 11 has approximate center coordinates $\alpha_{1950} = 15^h48^m11^s$, $\delta_{1950} = -03°57'14''$, and a local standard of rest (LSR) velocity of about 2.5 km s^{-1} (CB); it is thus near the larger dark cloud L 134 and possesses about the same radial velocity. Franco (1989) used Strömgren photometry to estimate the distance to L 134 to be 110 ± 10 pc, based on the location of the first step in an extinction versus distance diagram. Alternatively, LBN 11 could be associated with the ρ Oph molecular cloud which dominates the Upper Scorpius region. Distances to the front, center, and back of the Upper Sco dust clouds were estimated to be 80, 125, and 170 pc, respectively, by de Geus *et al.* (1989), from analysis of the reddening of stars in the Sco OB2 region. Here, we adopt a distance of 110 pc to LBN 11, based on the L 134 association.

The cloud has an optically cataloged angular extent of about 11×7 arcmin (0.35×0.22 pc) extending along a position angle of 90° (CB). The cloud is partially connected to clouds to the north–east and north–west, evidence of these appear in the CO and *IRAS* maps (see below). The position angle of latitudes parallel to the Galactic plane is 40° at the location of LBN 11, hence the cloud is not aligned along or perpendicular to the Galactic plane.

TABLE 1. Summary of optical polarization measurements.

Star No. (1)	α (1950) (2)	δ (1950) (3)	m_g [mag] (4)	P [%] (5)	σ_P [%] (6)	χ [°] (7)	σ_χ [°] (8)
1	15 47 41.6	−04 02 24	12.0	2.62	0.08	86	1
2	15 47 45.5	−04 00 27	14.4	1.44	0.16	83	3
3	15 47 50.5	−04 02 05	15.5	3.38	0.39	87	3
4	15 47 50.8	−03 53 14	14.0	2.90	0.28	76	3
5	15 47 55.6	−03 54 04	10.5	2.09	0.13	87	2
6	15 48 01.4	−04 00 52	14.1	3.04	0.20	66	2
7	15 48 04.1	−03 53 10	14.6	3.27	0.40	74	4
8	15 48 20.0	−03 59 47	12.6	2.30	0.15	76	2
9	15 48 30.3	−03 53 12	16.9	3.00	1.32	94	13
10	15 48 31.7	−04 01 30	10.8	2.25	0.08	82	1
11	15 48 33.9	−03 54 28	13.4	1.70	0.19	79	3
12	15 48 33.9	−04 01 45	14.1	2.51	0.36	70	4
13	15 48 38.3	−03 52 23	13.4	2.54	0.23	87	3
14	15 48 42.6	−04 00 41	16.2	2.62	0.47	74	5
15	15 48 43.7	−03 56 53	16.2	3.16	1.07	85	10
16	15 48 46.1	−03 52 39	14.2	2.64	0.25	84	3

With the exception of being cataloged by Lynds and CB, this cloud had not been selected for detailed study before 1988. However, because of its proximity and convenient, high-latitude location (during Galactic "dead time"), it was selected for observation during an optical polarization run with the Minipol instrument.

2.2 Optical Polarimetry

The polarimetric observations were performed during 8–10 June 1988 using the Minipol optical polarimeter (Frecker & Serkowski 1976) on the 1.5 m (61″) telescope of the University of Arizona Observatories on Mt. Bigelow, Arizona. The data were collected through a 15″ aperture and a g band filter ($\lambda_0 \sim 5500$ Å, $\delta\lambda \sim 500$ Å). Internal calibration via a Glan prism established the polarization efficiency at 98.2%. Observations of HD 155197 ($P = 4.627$, $\chi = 105°.13$; Tapia 1988) were used to establish the instrumental offset angle; the absolute positional uncertainty was under one degree. During this observing run, several Mathewson & Ford (1970; hereafter MF) stars were observed to test their suitability as intermediate magnitude polarization standards (Clemens & Tapia 1990), further verifying the quality of the LBN 11 stellar observations.

Table 1 lists our measured polarizations for stars in the vicinity of LBN 11. The stars are ordered by right ascension and their approximate g band magnitudes are listed. However, no atmospheric extinction or color corrections have been applied, so the listed magnitudes should only be used as relative brightness indicators for identification purposes. Columns (5) and (6) list the percentage polarizations and their 1σ uncertainties. Columns (7) and (8) list the polarization position angles on the sky and the 1σ uncertainty in the angles. Most of the angular uncertainties are around 3°, except for two of the faintest stars, which have larger uncertainties.

All of the stars exhibit large values of linear polarization, with position angles that are quite similar. In Fig. 1, the histogram of observed polarization percentages for the stars is shown and may be compared to similar histograms of the polarizations measured for stars in the vicinities of the B 216-217 and B 18 regions of Taurus (Heyer *et al.* 1987; Vrba *et al.* 1988) and for the 15 dark clouds studied by Myers & Goodman (1991). The mean polarization of the stars towards LBN 11, $2.38 \pm 0.04\%$, is between the means for B 216-217 ($2.09\% \pm 0.13\%$) and B 18 ($2.68\% \pm 0.14\%$). These values are all much larger than would be expected from grain alignment in the more diffuse, hot intercloud medium, arguing that these clouds are involved in generating the linear polarization via an embedded magnetic field.

Figure 2 shows the histogram of the derived polarization position angles for LBN 11 stars. The narrowness of the peak in the histogram suggests that the direction of the magnetic field lacing the molecular cloud is fairly uniform. The peak in the histogram for LBN 11 is much narrower (dispersion $\sim 6°$) than the corresponding peaks for B 18

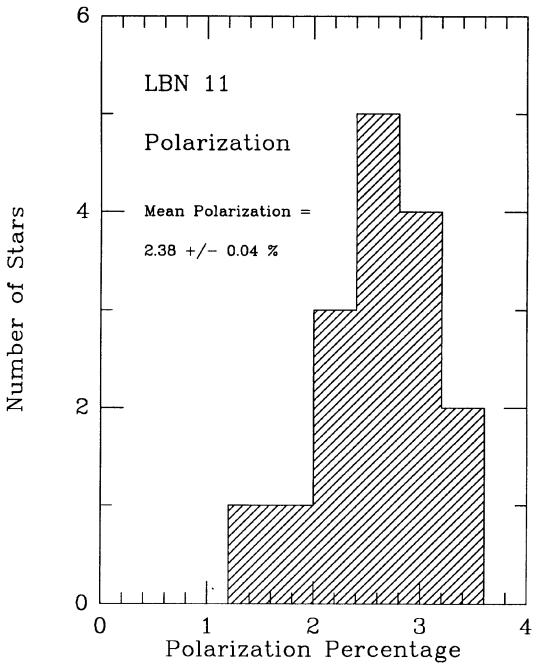

FIG. 1. Histogram of the percentage polarizations measured for 16 stars near LBN 11.

(21°) and B 216-217 (25°), and narrower than all of the histograms in the Myers and Goodman sample.

2.2.1 Local galactic magnetic field direction

The compilation of stellar polarizations of MF has been generally recognized as useful for indicating the distribution of the Galactic magnetic field over large spatial scales. In the vicinity of LBN 11 there are five MF stars within 6°, as listed in Table 2. The first two stars in this distance-ordered list exhibit rather small polarizations and have position angles far from the mean of the LBN 11 stars. However, the remaining stars in Table 2 have position angles very close to the average found for LBN 11, and the final two stars exhibit fractional polarizations nearly as large as those associated with the stars surrounding LBN 11. Distances to the last two stars were derived by MF by assuming a relation between the polarization and color excess. This renders their distances considerably less certain than those for the other stars. Nevertheless, the similarity of polarization properties of the MF stars to the LBN 11 stars for distances greater than 105 pc is consistent with a distance of 110 pc for the globule, and with a magnetic field lacing LBN 11 which is parallel to the local Galactic magnetic field.

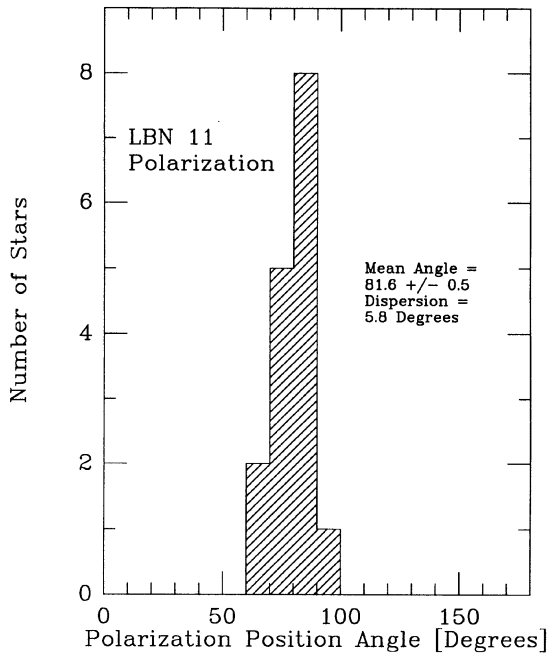

FIG. 2. Histogram of the polarization position angles measured for 16 stars near LBN 11.

2.2.2 Scale length of the magnetic field directional dispersion

In order to examine details of the magnetic field associated with the cloud, the correlation of the stellar polarization position angles was examined. For each pair of stars, a weighted mean absolute value of position angle difference was calculated, with a weighting inversely proportional to the summed squares of the position angle uncertainties.[3] The differences were averaged into bins of the log of the separation between the stars in each pair. Values of the mean angular difference as a function of the log of the separation are presented in Fig. 3. (The angular separations between the optical polarizations were converted to physical distance by adopting 110 pc as the distance to the cloud. As the cloud is the likely source of the polarization enhancements seen for these stars, this choice is appropriate.)

The figure shows that the mean difference in polarization position angle between two independent lines of sight rises to a maximum of about 10–12° for lines of sight separated by about 0.1 to 0.2 pc, and declines thereafter. Although the uncertainties in the bins for distances smaller than 0.2 pc are substantial, the decline on the large size side is very significant and serves to limit the magnetic field directional dispersion length scale. Also, the values in the first and fourth bins differ by a factor of 3.7 times the root square sum of their individual squared uncertainties, hence there is also a lower limit to the length scale. As will be shown below, the mean size scale (0.1–0.2 pc) also corresponds to the mean sizes of the ^{12}CO and ^{13}CO clumps found in the cloud.

2.3 Millimeter Molecular Line Mapping

LBN 11 was observed in the $J=1-0$ lines of ^{12}CO (hereafter CO), ^{13}CO, $C^{18}O$, and HCO^+ using the 14 m radio telescope of the Five College Radio Astronomy Observatory (FCRAO) near New Salem, Massachusetts, dur-

[3]This correlation is essentially the square root of the position angle structure function.

TABLE 2. Mathewson and Ford stars near LBN 11.

HD No.	Distance	A_V	P	χ
	[pc.]	[mag.]	[%]	[°]
(1)	(2)	(3)	(4)	(5)
139137	28	0.8	0.99 (0.03)	70 (1)
145206	105	0.1	1.07 (0.03)	105 (1)
140873	145	0.3	0.86 (0.03)	84 (1)
143396	159	1.3[a]	1.79 (0.05)	88 (1)
142863	182	1.2[a]	1.72 (0.06)	85 (1)

[a] – extinction was derived from the percentage polarization (MF).

ing the two periods 10–13 November 1989 and 15–17 December 1989. The nominal central position adopted for making the maps was $\alpha_{1950}=15^h48^m01^s$, $\delta_{1950}=-03°53'29''$.

Pointing was checked frequently on IRC+10216, Mars, Jupiter, and Saturn. Continuum slices through Jupiter and Saturn were used to determine a beamwidth of 45″ and a main beam efficiency of 43% at the CO wavelength. The first sidelobes were also visible in the cuts through Jupiter, and were found to contain approximately 41% of the total forward efficiency. Hence, for cloud structures smaller than the first sidelobes, the coupling efficiency η_C is about 43%, while for structures larger than the first sidelobes, η_C rises to about 84%. Because of this size dependence, we have elected to show antenna temperatures corrected for atmosphere and other gain effects, *but uncorrected for source coupling* in the data presentations. System temperatures were typically around 750 K SSB at CO, 650 K at ^{13}CO, 430 K at $C^{18}O$, and 370 K at HCO^+. Atmospheric opacities were determined from antenna dips, and each spectrum was calibrated using a chopper vane, corrected for the sky temperature determined from the dips.

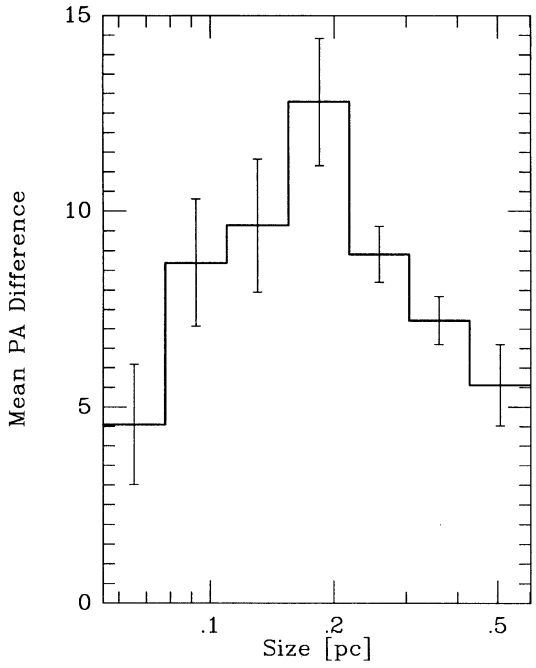

FIG. 3. Plot of the magnetic field directional dispersion vs scale size. The correlation was computed as the weighed mean two-point angular difference between stellar polarization measurements. The error bars reflect the uncertainties in the weighted means for each scale size bin.

For the LBN 11 observations, a 100 kHz per channel filter bank was combined with a digital spectrum expander to yield an effective velocity resolution of about 65 m s^{-1} (25 kHz) at the CO and ^{13}CO wavelengths, about 34 m s^{-1} (12.5 kHz) at the $C^{18}O$ wavelength, and 42 m s^{-1} (also 12.5 kHz) at the HCO^+ wavelength. The weak $C^{18}O$ and HCO^+ spectral lines were smoothed with a Gaussian filter to 68 and 82 m s^{-1} resolution before reduction, in order to boost their signal-to-noise ratios. All spectra were collected by frequency switching. (There was no contamination from the telluric CO line, whose LSR velocity during these observations was about 28 km s^{-1}.) A total of 99 positions was observed in the CO line, mostly over a 2 arcmin grid, with some positions in the center of the grid sampled at 1 arcmin spacing. A total of 58 ^{13}CO positions was observed, mostly with 1.5 arcmin spacing, though some of the central positions have 45 arcsec spacing. Fourteen $C^{18}O$ positions were observed toward the central region of the cloud at 1 arcmin spacing. Three central positions, spaced by 45 arcsec in declination, were observed in HCO^+, as well as in all three CO isotopes.

CS ($J=2-1$; 98 GHz) and SO ($J,K=3,2-2,1$; 99.3 GHz) observations of the central 4′.5 of the cloud were made during 25–27 October 1991 at FCRAO using the newly commissioned 15-beam receiver QUARRY (Erickson *et al.* 1992). The data were collected in position switched mode, against positions separately verified to be emission free. The filter resolution used was 250 kHz, or about 0.76 km s^{-1} per channel. A special mapping mode for QUARRY was used to generate final maps with 12 Declination (Dec.) by 10 Right Ascension (R.A.) samples on a 25″ grid (i.e., Nyquist sampling for the 53″ beamsize measured on Jupiter). The spectra had baseline noise levels of 0.08 K T_A^* per channel. At the CS frequency the main

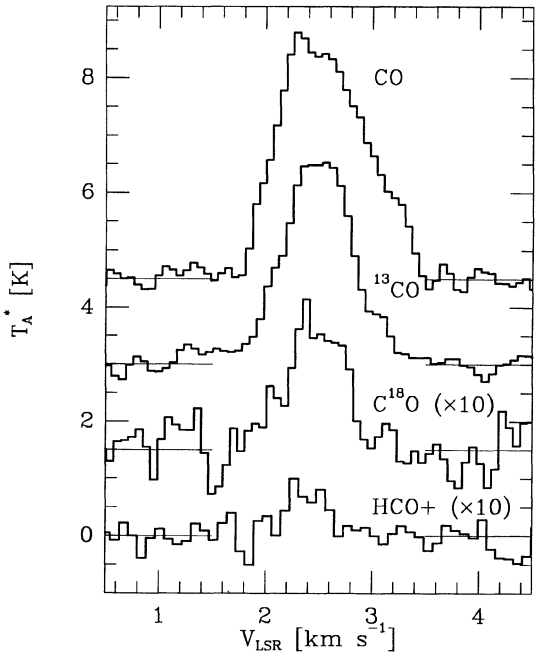

FIG. 4. Spectra obtained toward the $(\Delta\alpha,\Delta\delta)=(1',-2')$ position in LBN 11.

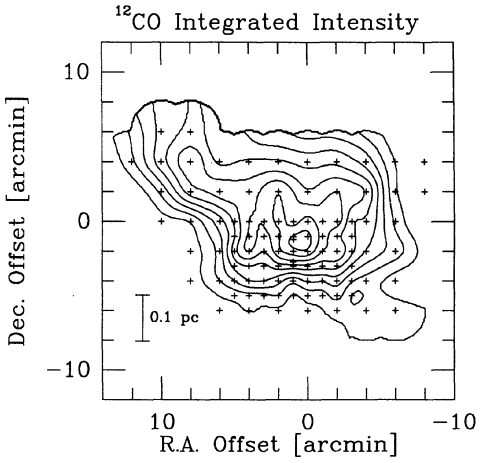

FIG. 5. Contour map of the CO integrated line intensity vs positional offset from $\alpha_{1950}=15^h48^m01^s$, $\delta_{1950}=-03°53'29''$. The lowest contour represents an integrated intensity of 0.5 K km s^{-1} ($\int T_A^* dV$), and subsequent contours are stepped by the same value. Plus signs denote positions observed for CO. The CO emission is strongest just south and east of the (0,0) position. A tongue of emission extends to the northeast. The southern cloud boundary is much sharper than the northern boundary. Along the northern boundary, edge effects in the contouring routine have lead to artificially closed contours.

beam efficiency was measured to be 0.50, and we assume the same value applies to the SO observations.

Figure 4 shows the lines detected toward an offset ($\Delta\alpha$, $\Delta\delta$) = (1′, −2′) from the fiducial map center. (This location corresponds roughly to the actual cloud center.) The C^{18}O and HCO$^+$ lines have been scaled up by a factor of ten for clarity. It should be noted that the CO, while relatively broad compared to the other lines, is actually quite narrow, with a FWHM of only about 1 km s^{-1}. Further, the ^{13}CO is quite strong, nearly as strong as the CO line. It appears to be somewhat flat-topped, and is centered at a velocity distinct from that of the CO line peak. This suggests that self-absorption of the CO line may be present at this position, attesting to a high column density of quiescent gas along this line of sight. Finally, note that the C^{18}O and HCO$^+$ lines are very weak at this location, indicating that there is relatively little high density gas along this direction. (The HCO$^+$ was especially difficult to detect, with the line shown representing more than four hours of integration time on source.)

In Fig. 5, the integrated intensity of the CO line in K km s^{-1} (uncorrected for η_C), is presented; plus signs indicate the locations of the positions observed in this line. The strongest emission occurs near ($\Delta\alpha$, $\Delta\delta$) = (0.5, −1.5). In integrated intensity, the cloud exhibits a single CO core, and is somewhat elongated, though not quite along the position angle cataloged optically. Figure 6 is a map of peak CO line temperature, again uncorrected for source coupling. Here, a second peak at (8,2) is seen, as are minor peaks at (2,2) and (−3,2).

If we assume η_C for the CO lines is about 65% (that appropriate to the main beam plus some side lobe filling) and further assume that the CO lines are optically thick and thermalized, the peak cloud gas temperature is about 10.3 K at position (1, −2). Values nearer 5 K are indicated in the cloud periphery and almost certainly indicate subthermal excitation of the CO in the lower density gas, and not the physical gas temperature. The bulk of the cloud

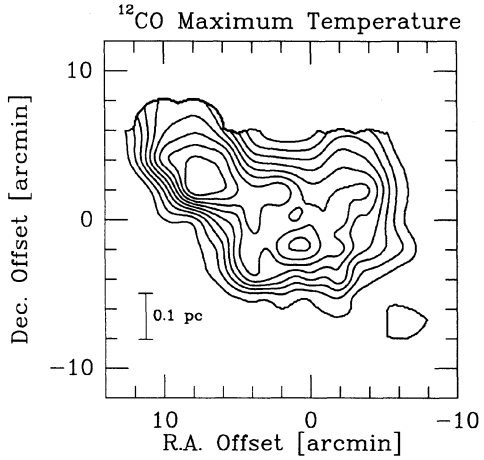

FIG. 6. Contour map of the CO peak line temperature (T_A^*) for LBN 11 on the same angular scale as Fig. 5. The lowest contour corresponds to 0.5 K and the contour steps are the same as that value. In this map, there are two zones of enhanced gas temperature, one near (1, −2) and another near (8,2). These two peaks have approximate gas temperatures of 10.3 and 11.8 K, respectively, assuming η_C of 65%.

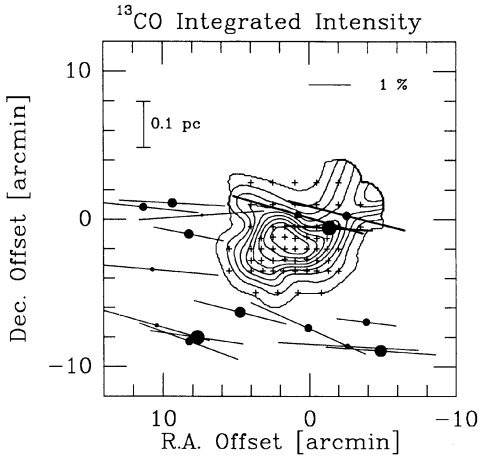

FIG. 7. Combined contour map of ^{13}CO integrated line intensity and polarization results for the 16 stars measured optically. The contours start at a value of 0.25 K km s^{-1} (T_A^*). The filled circles show the positions and approximate relative brightnesses of the optical polarization stars. The lines through the stars indicate the position angles and degrees of polarization measured. A scale showing the length representing a 1% polarized star is in the upper right. Three stars whose projected positions are within the ^{13}CO contours have had their polarization lines emboldened for clarity only. Note that the ^{13}CO peak emission occurs roughly midway in the stellar positional distribution, corresponding to the maximum visual extinction region.

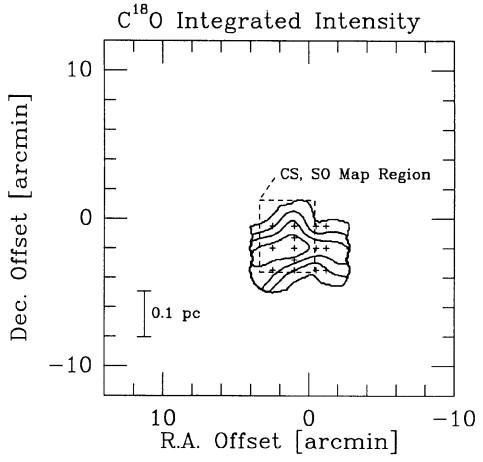

FIG. 8. Contour map of the C^{18}O integrated line intensity for LBN 11 on the same scale as in Fig. 5. The lowest contour level corresponds to 0.025 K km s^{-1} (T_A^*), and the contour step size is the same as that value. The dashed box indicates the size and location of the region mapped in CS and SO using QUARRY.

shows temperatures between 8 and 10 K, and we therefore estimate a mean temperature of 9 K for the gas in this cloud, similar to many other dark clouds and Bok globules.

Figure 7 presents the ^{13}CO integrated line intensity, with plus signs denoting the locations at which the spectra were observed. Additionally, the positions, magnitudes, polarization position angles, and percentages are shown for the 16 stars probed for optical polarization. The ^{13}CO map suggests a single core, although it should be noted that the (8,2) region, which appears as a secondary peak in the CO temperature map, was not sampled in ^{13}CO. The core appears to be partially elongated, although the position angle of the elongation depends on the contour level chosen. Generally, however, the outer contours indicate an elongation in the east–west direction, roughly parallel to the optical polarizations.

The dense core seen in the ^{13}CO map has half-power full widths of about 7×5 arcmin, corresponding to about 0.22 ×0.16 pc at a distance of 110 pc. The peak ^{13}CO line intensity is about 3.5 η_C^{-1} and the integrated intensity is 2.25 η_C^{-1} K km s^{-1}. Under the assumptions of η_C=0.65 and Local Thermodynamic Equilibrium (LTE; Dickman 1978) the ^{13}CO intensities correspond to a peak line opacity of 2.1 and a column density of 8.1×10^{15} ^{13}CO cm^{-2}. For a conversion ratio between ^{13}CO and H_2 appropriate for dark clouds of 2.2×10^{-6} (Dickman 1978), the H_2 column density, $N(H_2)$, is 3.7×10^{21} cm^{-2}. If the cloud is of uniform density and prolate in shape, the inferred mean volume density is 7700 H_2 cm^{-3}. For any radially decreasing gas density distribution, this average volume density is a lower bound on the peak volume density in the cloud core.

Figure 8 shows the integrated intensity of the C^{18}O line and the positions observed. Although a single core is present in the region studied, it should be noted that the lines are very weak and generally do not exhibit single, simple profiles. This last issue is discussed in Sec. *3.4*, below.

Figure 8 also shows the location and size of the region mapped in CS and SO using the QUARRY receiver. Maps of the integrated intensities of these lines are shown in Figs. 9 and 10. Because high dispersion spectrometers for all 15 QUARRY beams were not yet available, the CS and SO observations were conducted using the rather coarse 250 kHz filters. As a result, the lines are not resolved, and

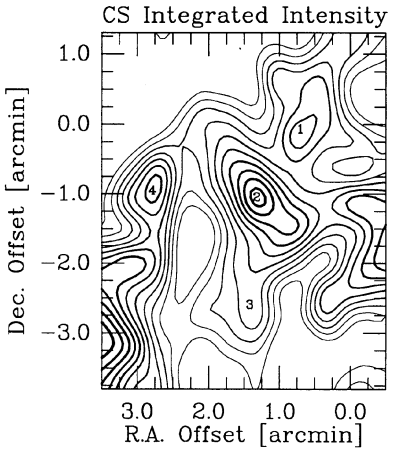

FIG. 9. Contour map of CS (J=2−1) line integrated emission from the core of LBN 11. The lowest contour corresponds to 0.05 K km s^{-1} and subsequent contours are stepped by the same amount. Cataloged features have numbered centers.

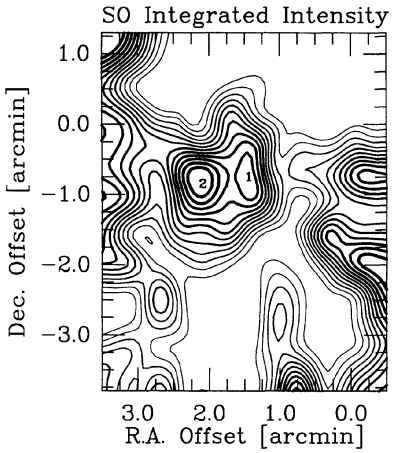

FIG. 10. Contour map of SO ($J,K=3,2-2,1$) emission over the same region as in Fig. 9. The lowest contour corresponds to 0.05 K km s^{-1} and subsequent contours are stepped by the same amount.

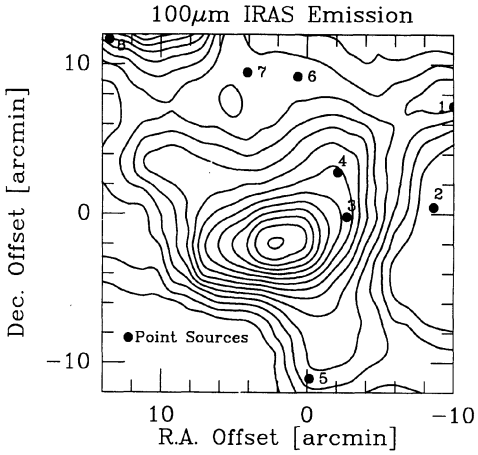

FIG. 11. Contour map of *IRAS* 100 μm emission for LBN 11 on the same scale as for Fig. 5. The lowest contour corresponds to 1.0×10^{-9} W m^{-2} sr^{-1} and the contour step size is five times that value. No point sources appear near the core region of strongest 100 μm emission.

specific line intensities, widths, and center velocities are unknown. However, channel maps were constructed and significant emission was detected in two channels for each molecule. The maps in Figs. 9 and 10 were constructed from the integrated intensities in these two channels. Features were detected above 2σ at multiply connected positions in both CS and SO. Since all of the features seen were small, the maps were corrected for the measured value of the main beam efficiency at CS, that is $\eta_C=0.50$.

In Fig. 9, the CS observations reveal emission arising from at least three, and possibly as many as five distinct regions. Four of the regions were well-delineated in the map. The observed properties of these four regions are listed in Table 3. The table lists a molecule and region identifying number (1), the ($\Delta\alpha$, $\Delta\delta$) offset from the CO mapping center (2 and 3), the peak integrated intensity (4), the full-width at half power of the feature, measured along its major and minor axes (5 and 6), and the approximate position angle of the major axis (measured east from north; 7).

Figure 10 shows the corresponding SO emission map. It also exhibits multiple structures. The central, brightest feature is essentially resolved into two regions of rather different characteristics; the SO properties of these two regions are also listed in Table 3 and their identifying numbers printed in Fig. 10. In the table, under the "Notes" column, cross references indicate that regions CS-2 and SO-1 are likely to be related because of their significant spatial overlap. However, the strongest SO component resides in a region remarkably free of CS emission. Since CS and SO have similar excitation requirements (thermalization densities near 10^6 cm^{-3}), the different CS and SO spatial distributions may be due to inhomogeneities in the cloud chemistry. This has been claimed for the CS and SO distributions in the nearby L 134N (L 183) cloud by Swade (1989).

2.4 IRAS Data

As part of a project to obtain *IRAS* co-added survey images of all 248 clouds in the CB catalog (CYH), 12, 25, 60, and 100 μm coadded images for LBN 11 were gener-

TABLE 3. Summary of CS and SO emission region properties.

Region Number	Δ RA [arcmin]	Δ Dec [arcmin]	$\int T_R dV$ [K-km s^{-1}]	a [arcmin]	b [arcmin]	P.A. [°]	Notes
(1)	(2)	(3)	(4)	(5)	(6)	(7)	
CS–1	0.75	−0.10	0.28	0.94	0.56	−25	
CS–2	1.25	−1.15	0.40	1.22	0.53	45	SO–1
CS–3	1.30	−2.50	0.20	0.78	0.53	10	
CS–4	2.75	−1.00	0.32	1.00	0.41	−5	
SO–1	1.50	−0.75	0.40	0.88	0.34	20	CS–2
SO–2	2.15	−0.85	0.44	0.75	0.56	−5	

TABLE 4. *IRAS* point sources near LBN 11.

Source No. (1)	α (1950) (2)	δ (1950) (3)	S_{12} [Jy] (4)	S_{25} [Jy] (5)	PSC Name
1	15 47 20.7	−03 46 17	0.58	1.53	15473−0346
2	15 47 26.6	−03 53 01	0.11	< 0.07	
3	15 47 50.2	−03 53 40	0.26	< 0.07	
4	15 47 52.7	−03 50 41	0.07	< 0.07	
5	15 48 00.4	−04 04 31	0.11	< 0.07	
6	15 48 03.5	−03 44 18	0.33	0.63	15480−0344
7	15 48 17.4	−03 44 02	0.29	< 0.07	
8	15 48 55.0	−03 41 49	0.12	< 0.07	

ated at the Image Processing and Analysis Center (IPAC) in Pasadena, CA. These images have angular resolutions of about 1′ at the shortest wavelengths, growing to 2–3′ at the longer wavelengths. Figure 11 presents part of the 100 μm image containing LBN 11, and shows the extended presence of the globule itself and low-level extensions to nearby clouds. At the angular resolution of the image, only a single core appears in LBN 11, but the extended nature of the 100 μm emission indicates that we are seeing the thermal emission from extended cool dust and not from an unresolved point source.

The 12 and 25 μm images were median filtered (with kernel size of 16 arcmin) and subtracted from the originals in order to enhance the sensitivity to faint point sources. Eight point sources were found within the boundary of Fig. 11, as indicated by dots and identifying numbers. Information concerning the sources is provided in Table 4. The fluxes listed were obtained using the POLYPHOT package within IRAF.[4] The limits listed at 25 μm are the 3σ limits appropriate for the area of the other point sources detected. Two of the eight point sources have *IRAS Point Source Catalog* (PSC) entries, as indicated in Table 4, and the PSC fluxes and the fluxes measured from the coadded images agree to better than 20%. The coadded coordinates were computed relative to the PSC coordinates for source 6; hence the source 6 coordinates *are* the PSC coordinates. Since the difference between the coadd and PSC coordinates of source 1 is 10 arcsec, we believe that the other source coordinates are likely accurate to better than about 20 arcsec.

Source 1 is associated with a visual magnitude 6.8 B9 star, while source 6 is a known quasar. The spectral indices for five of the remaining six sources are typical of normal (shell) stars and they are therefore surely background objects. The spectral index of source 4 (the faintest 12 μm source) could be as flat as that of a T Tauri star, but if the source is embedded in LBN 11, it is remarkably faint at all *IRAS* bands ($L_{IRAS} < 0.003 L_{\odot}$).

We conclude that there are no embedded young stars in LBN 11 to 3σ 12 and 25 μm limits of 0.03 and 0.07 Jy, respectively. The corresponding luminosity limits at a distance of 110 pc sum to a value of 0.0024 $L_{\odot}$, much fainter than the bolometric luminosity of an embedded M5 star.

By combining the 60 and 100 μm *IRAS* images along with a single temperature modified blackbody model with λ^{-1} emissivity (CYH), a mean dust temperature of about 20–21 K was deduced from the *IRAS* data. As the dust traced by *IRAS* preferentially samples the warmest portions of the dust temperature distribution, and misses some 90% of the coolest grain mass (CYH), these temperatures are upper limits for the mean cloud dust temperature. Surprisingly, the inferred gas temperature, 8–10 K, and the *IRAS* upper limit to the dust temperature, 20 K, are *closer* to each other for this cloud than for most of the globules studied by CYH, possibly because of the remoteness of the globule from heating sources (which tend to be more concentrated in the Galactic plane). The central 100 μm dust opacity is about 4.7×10^{-4}, fairly typical of the small globules (CYH).

The *IRAS* emission per hydrogen column density was estimated for LBN 11 by comparing the peak 100 μm emission value (7.34 MJy sr^{-1}) to the H_2 column density traced by ^{13}CO. The value of $I_{100}/N(H_2)$ so obtained is 0.18 MJy sr^{-1}/(10^{20} H_2 cm^{-3}), similar to the values reported for dark molecular clouds (Snell *et al.* 1989). The total *IRAS*-traced, far-infrared luminosity for LBN 11 is only 0.2 $L_{\odot}$, which is about a factor of 20 below that expected for a small cloud embedded in the mean interstellar radiation field of the Galactic plane (CYH). Since there are no embedded sources and the dust is very cold, much of the dust luminosity is likely emitted at wavelengths longer than sampled by the *IRAS* bands.

The radial density distribution of dust in LBN 11 was deduced by Yun & Clemens (1991) as part of a 12-cloud *IRAS* study of Bok globules. LBN 11 was found to exhibit

[4]IRAF is distributed by National Optical Astronomy Observatories which are operated by the Association of Universities for Research in Astronomy, Inc., under contract to the National Science Foundation.

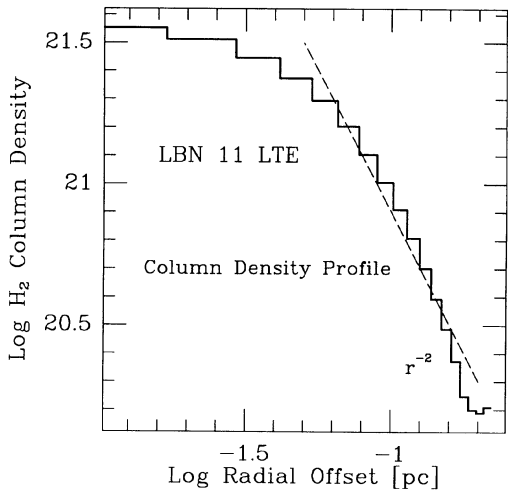

FIG. 12. Log–log plot of H_2 column density vs offset from the center of LBN 11. This profile is the azimuthal average of the column density image computed from the CO and ^{13}CO observations. The dashed line indicates the radial behavior of an r^{-2} power law distribution.

a column density power law with a radial exponent of -1.0 ± 0.1. The corresponding volume density power law exponent of the radius was estimated by Yun and Clemens to be -1.8 ± 0.1 for this cloud.

3. DISCUSSION

3.1 Cloud Density Structure and Cloud Mass

An H_2 column density map was computed from the CO peak temperature, ^{13}CO peak temperature, and ^{13}CO integrated intensity maps. The map looks virtually identical to the ^{13}CO integrated intensity map; it shows a single central peak of column density 4×10^{21} H_2 cm^{-2}, and confirms the generally optically thin nature of the ^{13}CO emission. The map was integrated to yield a total cloud mass of 1.48 $\mathcal{M}_\odot$ for the portion of the cloud mapped in ^{13}CO.

We next sought to create a representative spherically symmetric model for the cloud. The starting point was an azimuthally averaged column density profile computed from the column density image. The resulting profile is displayed in log–log form as Fig. 12. The innermost few bins are certainly affected by both limited angular resolution and the nonsymmetric distribution of the gas in the core of the cloud. Beyond the radii where beam resolution effects are important, the decrease in inferred LTE column density is not well matched by any single power law (for more discussion of the expected functional forms see Dickman & Clemens 1983, or Turner *et al.* 1992). In our model, we approximated this profile as a set of three connected power laws and a central uniform value of column density, equal to the observed maximum column density value. Integration of the model column density to a radius of 0.3 pc (the limit of the observed profile) yielded a mass of 1.66 $\mathcal{M}_\odot$, in good agreement with the actual integration of the column density image. The peak H_2 volume density in this model is about 3×10^4 cm^{-3}, averaged over one beam size. This is in good agreement with the CS and SO analyses of Sec. *3.2*, below. The total cloud mass was then estimated by continuing the outer column density power law (of radial power law index -3) to infinite offset. The resulting total mass is 2.0 $\mathcal{M}_\odot$.

Masses computed under the LTE assumption tend to underestimate total mass whenever either ^{13}CO becomes optically thick or subthermally excited (Dickman 1978). Both likely occur for this cloud, with optical thickness present in the core and subthermal ^{13}CO excitation and lowered abundance occurring in the cloud periphery, due to photodissociation by external UV illumination from the interstellar radiation field. Hence, the 2 $\mathcal{M}_\odot$ estimated may be a lower limit to the total cloud mass. However, the use of LTE is generally not in error by more than about a factor of two (Arquilla & Goldsmith 1985), and given the presence of $C^{18}O$, HCO^+, CS, and SO in the cloud, we doubt that the CO isotopes are wildly underabundant.

3.2 Chemical Abundances

Detailed analyses were performed using the CO, ^{13}CO, $C^{18}O$, and HCO^+ spectra obtained toward the three central positions $(\Delta\alpha,\Delta\delta)=(1,-2.8)$, $(1,-2.0)$, and $(1,-1.3)$. The goals were to examine the kinematics of the various gas tracers and to probe their abundances.

These central spectra were each fit with single Gaussians using a nonlinear least squares approach. Analysis of the Gaussian fit results clearly showed the presence of detectable velocity gradients with declination offset in all four molecular lines. The sense of all of the gradients was the same, namely a decreasing radial velocity with increasing declination. The CO line gradient was 3.1 ± 0.3 km s^{-1} pc^{-1}, while the ^{13}CO, $C^{18}O$, and HCO^+ lines showed gradients a bit more than twice that value, at 6.5 ±0.3, 6.3 ± 0.7, and 7.0 ± 1.8 km s^{-1} pc^{-1}, respectively. It is especially noteworthy that the HCO^+ line, which probes the densest gas regions along the line of sight and as a result of its electrical charge could be tightly linked to the magnetic field lacing the cloud, is found to have kinematics virtually identical to the lower, neutral gas density tracers $C^{18}O$ and ^{13}CO. These gradients found for the core region of the cloud are due to rotation of the cloud, as shown in Secs. *3.3* and *3.4.5*, below.

An LTE analysis was performed using the lines of ^{13}CO, $C^{18}O$, and HCO^+, assuming that the CO line acts as the relevant excitation temperature indicator. For ^{13}CO, the peak line opacity was 2 and the total column density of ^{13}CO was 9.6×10^{15} cm^{-2}. For $C^{18}O$, the values were 0.05 and 2.7×10^{14} cm^{-2}, respectively, while for HCO^+ the values derived were 0.02 and 9.0×10^{10} cm^{-2}. The ratio of the ^{13}CO to $C^{18}O$ column densities had a mean over the three positions of 33, while the similar ratio of $C^{18}O$ to HCO^+ column density was 2900.

If the ^{13}CO and $C^{18}O$ are similarly excited and distributed and have relative elemental abundances in solar proportions, the expected column density ratio would have been 5.6 instead of 33. Several factors can influence the column density ratio. These include fractionation of the

^{13}CO (Dickman *et al.* 1979), isotope-selective photodestruction (Bally & Langer 1982), subthermal excitation of the $C^{18}O$ relative to ^{13}CO, and true abundance differences and variations within the cloud. Because the total optical depth to dissociating interstellar UV is not high for this cloud, *all* of these effects are likely operating.

It is worth comparing the ratio of ^{13}CO to $C^{18}O$ in LBN 11 to the same ratio in the small Bok globule CB 4 studied by Dickman & Clemens (1983). CB 4 exhibited a ^{13}CO to $C^{18}O$ column density ratio of 10 toward the central position of that cloud. Detailed line modeling could not account for such strong $C^{18}O$ lines there, and tended to produce ratios nearer the one reported here for LBN 11. Hence, instead of concluding that LBN 11 is $C^{18}O$ weak, the correct conclusion may be that CB 4 shows overly strong $C^{18}O$ lines for a small globule, perhaps because CB 4 is roughly five times more massive than LBN 11. Turner *et al.* (1992) also concluded that the $C^{18}O$ lines from CB 4 were strong, but were able to obtain correct line strengths from their polytropic cloud model.

However, the peak ^{13}CO column density in CB 4 is about a factor of 2.6 *lower* than the value found for LBN 11. This may imply that fractionation is more prevalent in LBN 11, or it may merely be due to a beam resolution effect (CB 4 is at 600 pc distance). Note that if ^{13}CO is more highly fractionated in LBN 11, our previous mass estimates may be too high.

Because HCO^+ has such a large dipole moment and because the mean cloud volume density is modest, we expect the species to be subthermally excited. However, as long as the excitation temperature is equal to or exceeds 4 K, some interesting limits can be inferred. If HCO^+ is well-mixed with the ^{13}CO and uniformly excited to at least 4 K, then even if the ^{13}CO is fractionated by a factor of 2 over its normal interstellar abundances, the inferred abundance of HCO^+ is less than 10^{-10} relative to H_2; this is at least a factor of five lower than seen elsewhere (Frerking *et al.* 1987) or modeled (Hasegawa 1987). Alternately, if the abundance of HCO^+ is as high as the lowest value modeled, 5×10^{-10} (Hasegawa), then the filling fraction of HCO^+ emitting gas is no more than 0.1–0.2, depending on the ^{13}CO fractionation.

While the observational findings of weak $C^{18}O$ and HCO^+ lines are secure, detailed chemical explanations of this weakness are suspect. As is shown below, the cloud *is* clumpy. Coupled with low UV opacities, this clumpiness may easily produce the line intensities observed without resorting to nonstandard chemistry. Nevertheless, we expect molecular abundances will vary significantly with depth into the cloud due to the UV penetration and the long times needed to reach chemical equilibrium.

The SO and CS line emission maps were interpreted with the goal of estimating the peak volume densities and masses traced by these molecules. The task was made more difficult by our lack of resolved line profiles, although reasonably firm limits can be established. The integrated line photometry presented in Table 3 was interpreted under the assumptions of optically thin lines which are uniformly excited. Swade (1989) concluded that CS and SO in the core of the nearby cloud L 134N (L 183) have excitation temperatures near 5 K. For this excitation temperature in LBN 11, the peak column densities of CS are 1.8, 2.5, 1.3, and 2.0×10^{12} CS molecules cm^{-2} for the regions CS-1, CS-2, CS-3, and CS-4, respectively, and 4.8, and 5.3×10^{12} SO molecules cm^{-2} for SO-1 and SO-2.

In massive molecular clouds, fractional abundances of CS are typically around 1×10^{-8} CS per H_2 while SO abundances are a few$\times10^{-9}$ (Irvine *et al.* 1987). However, Swade (1989) has found much lower abundances in the L 134N cloud: 7×10^{-10} for CS and 2×10^{-9} for SO. If we adopt his values, the peak hydrogen column densities toward the CS regions are 2.5, 3.6, 1.8, and 2.9×10^{21} H_2 cm^{-2}, and 2.4, and 2.7×10^{21} for the SO regions. Dividing these column densities by the mean sizes of the regions, leads to estimates of the mean volume densities in the inner parts of the regions of the order of 2.1×10^4 or $10^{4.3}$ H_2 cm^{-3}. This is very close to the values found in the ^{13}CO LTE analysis. Rough masses of the CS and SO emitting regions were estimated by assuming these mean densities prevailed over each of the regions detectable in these tracers. The total mass so traced is 0.27 $\mathcal{M}_\odot$, or 18% of the cloud mass traced by ^{13}CO.

3.3 Rotation Analysis

In order to probe the rotation of LBN 11, we fit the observed CO isotopic line center velocities with a solid body rotation model, similar to that of Heyer (1988). This planar fit returns the value and uncertainty of the rotational gradient (in km s^{-1} $arcmin^{-1}$) and the position angle and uncertainty of the associated angular momentum vector. Emission-weighted first velocity moments were used for the line center velocities and were weighted by the inverse squares of the resulting uncertainties (generally of the order of 80 m s^{-1}).

In Table 5, we summarize the two-dimensional rotation fits obtained for the entire cloud, as probed by CO, ^{13}CO, and $C^{18}O$. There are two fits for CO—one using all of the CO spectra, and one restricted to the region sampled by the ^{13}CO observations. The results for these two different CO data sets are not significantly different. Note that the CO and ^{13}CO maps return essentially identical values for the direction of the cloud rotation axis. However, the rotation gradient inferred from the ^{13}CO observations is roughly twice as large as that deduced from CO by considerably more than a 1σ margin, as was also noted for the cloud core spectra in Sec. *3.2*. The weaker $C^{18}O$ lines exhibit no detectable rotation, but only to very crude limits consistent with the ^{13}CO results. Line profile fitting would return much more accurate central velocities for Gaussian profiles, and hence would in principle be capable of probing the rotation state of the cloud much more accurately. However, as will be shown below, many of the lines in this cloud are more complex than single Gaussians, which renders single-line model results unreliable.

The angular difference between the CO rotation axis and the position angle of the magnetic field is $8\pm16°$. For ^{13}CO, this increases slightly to $12\pm11°$. The virtual

TABLE 5. Summary of cloud rotation analysis.

Molecule	Region	Observed Gradient (m s^{-1} arcmin^{-1})	Physical Gradient (km s^{-1} pc^{-1})	Rotation Axis Angle (Degrees)	Number of Spectra in Fit
^{12}CO	CO Map	41 (15)	1.3 (0.5)	−88 (19)	99
^{12}CO	^{13}CO Map	51 (17)	1.6 (0.5)	−90 (16)	68
^{13}CO	^{13}CO Map	116 (31)	3.6 (1.0)	−86 (11)	58
C^{18}O	C^{18}O Map	90 (27)	...	...	14

Notes: All uncertainties in parenthesis are 1 σ uncertainties.

coalignment of the magnetic field and angular momentum vectors strongly suggests that the field is tightly coupled to the periphery (and possibly the core) of the cloud. If the higher rotation gradient in the cloud interior indicated by the ^{13}CO data is accepted at face value, there are then several possible explanations for the higher gradient. The kinematic state of the core may simply reflect conservation of angular momentum in the absence of a magnetic field during core condensation, which requires essentially complete magnetic field leakage from the core. Alternatively, the cloud periphery may have been selectively braked by magnetic forces (since absolute field displacements grow larger with cylindrical radius for a solid body rotation curve). Finally, the entire cloud may be in a state of free torsional oscillation, with the core and periphery being out of phase (and possibly with different oscillation amplitudes). Note that torsional oscillations would be almost unavoidable if the observed shear motions are occurring within the gas containing the magnetic field (Arons & Max 1975); in this case, however, the wound-up field lines might produce a much more disordered polarization pattern than is observed (or might not, depending on line-of-sight superposition of polarization projections).

The moment of inertia and angular momentum were computed for a spherical cloud model of LBN 11, which treats the radial dependence of the H_2 volume density as a single power law (power law index −3). The model contains two cloud components, a core region, which is delineated by the strongest ^{13}CO emission, and an envelope. We chose a characteristic core radius of 0.1 pc, which corresponds to the location of the ^{13}CO half power emission. For the core region, we adopted the ^{13}CO rotation kinematics, while for the envelope the CO kinematics were adopted, both from Table 5.

The moment of inertia of the envelope is about 4.8 $\times 10^{-3}$ $M_\odot$ pc^2 and the angular momentum is 2.6×10^{-16} $M_\odot$ pc^2 s^{-1}, or 0.008 $M_\odot$ km s^{-1} pc, in the units of Goldsmith & Arquilla (1985; hereafter GA). These values are similar to those for the slowly rotating dark cloud B 68 studied by Martin & Barrett (1978; one of the GA clouds). The corresponding specific angular momentum J/M is about 0.0045 km s^{-1} pc for a characteristic diameter of 0.6 pc. This level of rotation is smaller than the levels seen for the strong rotors studied by GA.

The core, traced by ^{13}CO, is denser, extends over a smaller region, and rotates faster than the envelope. The derived moment of inertia, angular momentum, and specific angular momentum are 5.8×10^{-4} $M_\odot$ pc^2, 2.1×10^{-3} $M_\odot$ km s^{-1} pc, and 7×10^{-3} km s^{-1} pc, respectively. For a 0.2 pc diameter region, this rotation is consistent with the virial stability of an r^{-2} or steeper gas density distribution, as shown by GA.

Within the core region rotational, turbulent, and magnetic energies appear to be roughly comparable at about 8×10^{40} ergs (with the magnetic energy scaling as $[B/4$ μG$]^2$, and the turbulent energy computed from the C^{18}O line fitting of Sec. *3.4.4*, below). Thermal and gravitational energies are about 2–3 times larger. This places a fairly firm upper limit of about 7 μG on the mean magnetic field strength within the core region if the magnetic field self-energy is to be smaller than the gravitational potential energy.

Hence, the angular momentum content is not so high as to demand disruption of the cloud, nor so low as to allow the unimpeded collapse of the cloud core or envelope. This suggests that the cloud has existed long enough to reach rough equilibrium between rotation, turbulence, and embedded magnetic field strength. We infer that the cloud must be at least several sound crossing times old, that is, the minimum age of the cloud is several million years. Note that the rotation periods of the core and envelope are 2 and 4 million years, respectively.

3.4 CO Line Profile Analyses

The CO, ^{13}CO, and C^{18}O spectra have been obtained with exceedingly high velocity resolution and with good signal-to-noise levels. The line profiles at some positions are simple and Gaussian, while at other positions they are clearly composed of multiple line-of-sight components which overlap and sometimes self-absorb. In this section, we present some of the spectral line profiles and carry out two distinct analyses of all of the profiles. The first uses multiple Gaussians to fit the observed line profiles. These fit parameters are used to characterize the dynamical nature of the cloud in some detail. This analysis suggests that the number of distinct velocity features is large and that the regions producing the individual features are mostly

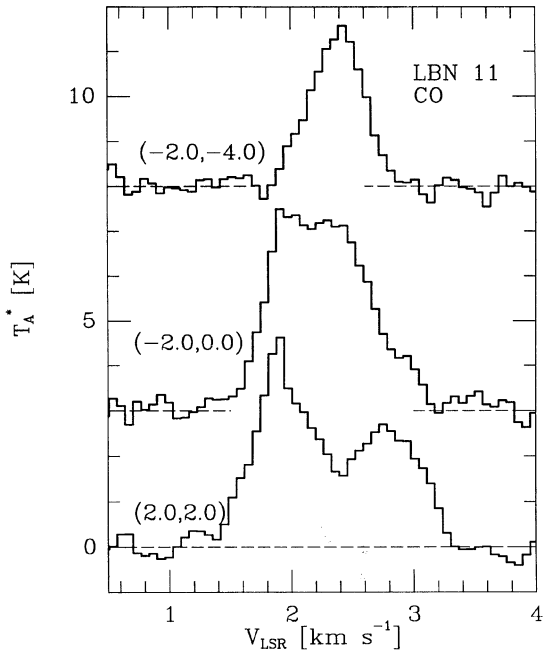

FIG. 13. Three CO spectra obtained towards different regions in LBN 11, chosen to highlight different line profile shapes. The positions observed are indicated to the left of the spectra as $(\Delta\alpha,\Delta\delta)$.

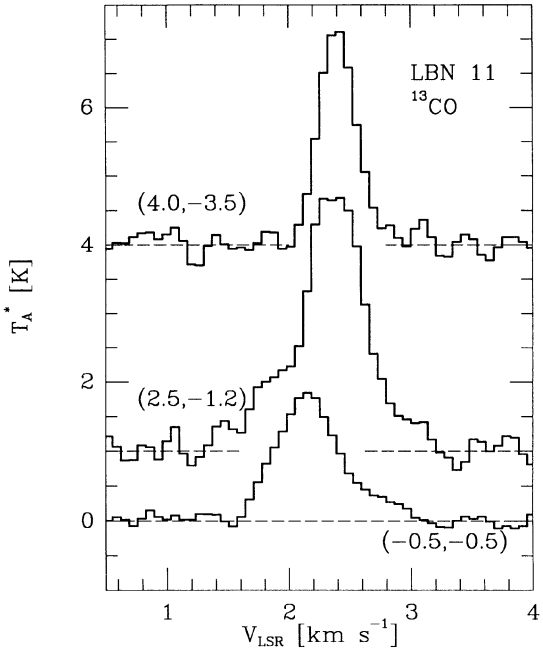

FIG. 14. Same as Fig. 13, but for ^{13}CO spectra from LBN 11, also selected to highlight diverse spectral line profiles.

subsonic in their internal kinematics. It also indicates that the cloud may be differentially rotating. The second analysis involves constructing channel maps of the cloud from the CO and ^{13}CO spectra. In these maps, many features are resolved in space and velocity, allowing a catalog of cloud clumps to be generated.

3.4.1 Spectral line profiles

Figure 13 shows three observed CO line profiles in LBN 11. In the uppermost spectrum, the CO line is singly peaked, has a velocity width of about 0.5 km s^{-1} (FWHM), and a centroid velocity of 2.4 km s^{-1}. The lowermost spectrum typifies the double lines also seen in the globule, with velocity separations of the peaks in excess of the FWHM widths of the individual components. The depth of the line emission between the peaks, and the shape of the central dip tend to rule out simple self-absorption for the spectrum shown and instead imply that along this line of sight, at least two distinct velocity components are present. The central spectrum in the figure reveals the complex nature of other well-resolved lines. The flat top of the line may be due to opacity effects or to the blending of two components. The wings of the line are dissimilar: the fast rise at low velocities is not mirrored in the slower, high velocity decline, on whose slope a marginally significant bump at 2.9 km s^{-1} is also seen.

Although by no means simple, the ^{13}CO lines are somewhat easier to interpret, probably because of their lower optical depths. Three ^{13}CO line profiles from LBN 11 are shown in Fig. 14. The uppermost contains a line which is very Gaussian and symmetric; it has a width of about 0.38 km s^{-1} and a center velocity of 2.4 km s^{-1}. This line is also very strong (as are many of the ^{13}CO lines), indicating that along some lines of sight, the ^{13}CO opacity is very large at certain velocities. The middle spectrum is composed of at least two components. One is strong and centered at about 2.4 km s^{-1}, the other much weaker and centered at a lower velocity. In the lowermost spectrum this situation is reversed: the strong component is at 2.1 km s^{-1} and the weaker one at a higher velocity.

The CO, and ^{13}CO, line profiles clearly exhibit the presence of multiple gas components for this cloud. Additionally, at positions where the lines are single, or have well-separated components, the component lines are themselves very narrow and Gaussian. The simplest explanation for this is that the cloud consists of numerous, kinematically simple units, moving in the collective magnetic and gravitational fields of the globule; the more complex line profiles would arise from the blending of these components along certain lines of sight. To pursue this picture, we attempted multiple Gaussian fitting of the cloud spectral line profiles. However, the presence of self-absorptions could confuse the interpretation of these results, and we turn to this issue next.

3.4.2 Self-absorption mapping

Self-absorptions in CO occur when cooler foreground gas absorbs photons formed deeper inside the cloud. Usually, self-absorptions indicate regions of very high optical depth, as are often seen toward dense cores, protostars, or YSOs. In Bok globules, self-absorptions occur frequently,

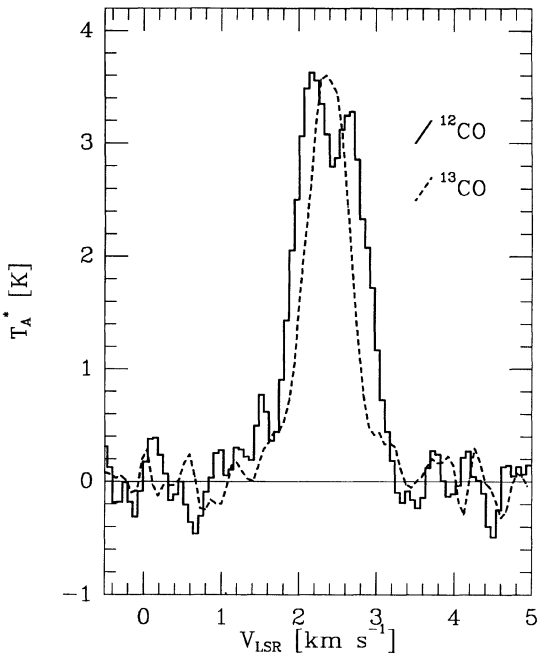

FIG. 15. CO and ^{13}CO spectra from the same region, showing the presence of strong self-absorption of the CO.

because the spectral lines are narrow, and because decreased excitation temperatures occur readily at the cloud periphery.

We searched LBN 11 for self-absorptions in the CO spectra, identifying them by the presence of a significant detectable dip near line center and a corresponding peak in the ^{13}CO line nearest the CO position (recall that the CO and ^{13}CO maps were collected on slightly different grids—see Sec. *2.3*). Figure 15 shows a comparison of the CO line seen toward the $(2,-1)$ position and the ^{13}CO seen toward $(1.7,-1.2)$. The CO line shows a central dip of about 0.8 K (T_A^*) at a velocity of 2.44 km s^{-1}. The ^{13}CO line there is as strong as the CO shoulders, indicating that the ^{13}CO line must also be optically thick. The presence of a ^{13}CO peak close in velocity to a CO dip is the signature of self-absorption of the CO.

Self-absorptions were clearly identified or strongly suspected toward about 20 positions in LBN 11. The mean velocity of the absorbing material was determined at each location from the CO spectra. The positions identified generally delineated two distinct simply-connected regions, whose properties are summarized in Table 6. The centers of the regions are listed as offsets of RA and Dec (columns 2 and 3) from the CO mapping center, the mean self-absorption velocity for each region is listed in column 4, and the dispersion in the self-absorption velocities for each region is listed in column 5. Note that the two regions are distinct in velocity. Finally, the semimajor and semiminor extents, and rough position angles of each region are listed in the last columns of the table. The mean diameters of these regions are 0.05 pc, about the same size as the SO and CS emitting regions.

While self-absorption can affect the number of components identified in a CO line profile, that number can only be in error by unity: we see no cases of multiple self-absorptions within individual CO spectra. However, the number of *visually* identified components in some of the multipeaked CO lines exceeds five. Also, in Fig. 14 we already presented evidence that the less optically thick ^{13}CO lines often show multiple line components.

3.4.3 Line profile fitting

We conclude that even with self-absorption artificially generating CO line multiplicity, there are bona fide multiple components in the CO and ^{13}CO profiles. We therefore performed multiple Gaussian fitting of all of the resolved spectral lines in LBN 11. The approximate centers and widths and numbers of components in each line were noted, and a program performed a nonlinear least-squares fit, returning Gaussian parameters and their uncertainties for each component, as well as the overall noise level of the residuals.

The fitting for each spectrum was begun using a single Gaussian. The residuals from that fit were then examined for the presence of excess emission or absorption (which would indicate that another component was likely present). If any was found, the fitting was repeated using two Gaussians, both fit simultaneously. The process of examining the residuals was repeated. If significant residuals were found, the fitting was tried again using three Gaussians. No fits with more than three Gaussians were performed, even though a few of the CO lines showed (generally weak) evidence of four or five components.

Figure 16 shows the observed spectrum, best fit, and residuals for the ^{13}CO line seen toward the $(-0.5,-0.5)$ position. Here only two Gaussians were needed to create a residual spectrum which is featureless across the emission line. The model Gaussian line center velocities for the features are 2.14 ± 0.01 km s^{-1} for the stronger component and 2.78 ± 0.05 km s^{-1} for the weaker one. The widths are

TABLE 6. Summary of CO self-absorption regions.

Region	Δ RA	Δ Dec	V_{LSR}	σ_V	a	b	P.A.
Number	[arcmin]		[km s^{-1}]		[arcmin]		[°]
(1)	(2)	(3)	(4)	(5)	(6)	(7)	(8)
SA-1	−2.5	−1.5	2.24	0.10	1.2	0.7	+30
SA-2	3.0	−1.5	2.44	0.11	1.0	0.6	−30

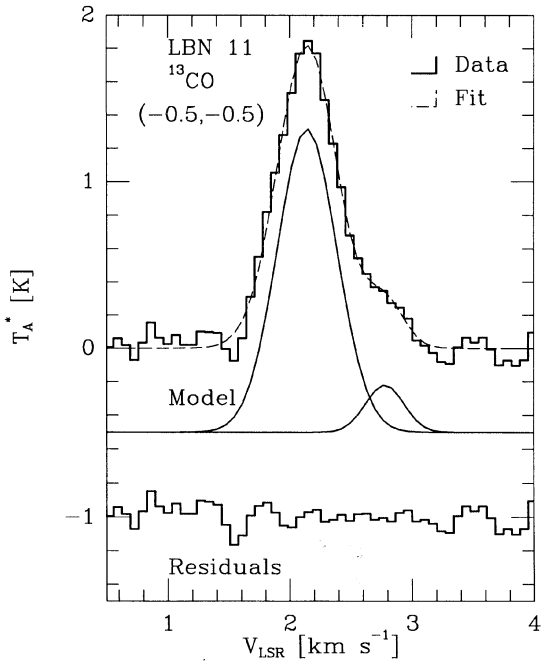

FIG. 16. Composite of several spectra illustrating the multiple Gaussian fitting analysis. In the uppermost spectrum, the solid line traces the observed ^{13}CO spectrum seen toward the (−0.5, −0.5) position. The middle spectra show the two model Gaussians fit to the observed spectrum. The dashed line in the upper spectrum superposes the combined model fit with the observed data. The residuals (observed minus fit) are shown as the lowermost spectrum. For this position, the two Gaussian fit provides an excellent representation of the observed line profile.

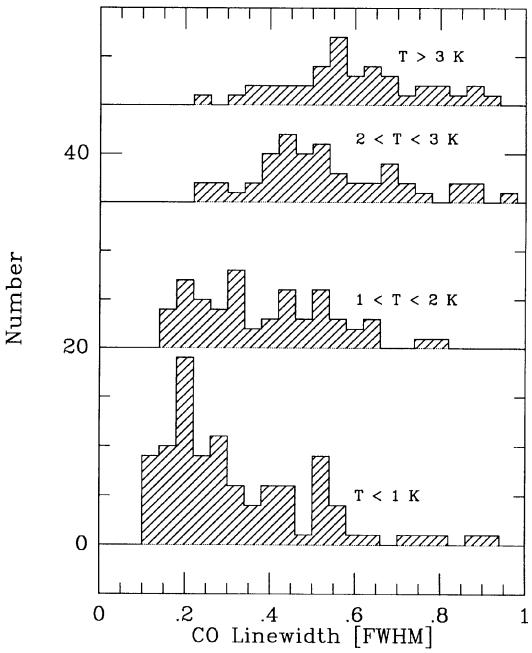

FIG. 17. Histograms of Gaussian component linewidths for the CO line profile fitting analysis. The histograms are separated vertically into four bins by their peak line strengths. The bottom histogram includes only those fitted Gaussian components whose strengths were less than 1 K T_A^*, while the uppermost histogram shows only the linewidths for components with line strengths greater than 3 K. Note that the widest fitted components generally occur for the strongest lines, as would be expected for saturation broadening of the very optically thick CO line.

0.58 ± 0.03 km s^{-1} and 0.37 ± 0.12 km s^{-1}, respectively. Note that the fitting returns highly precise central velocities (sometimes as low as 4–5 m s^{-1}). The rms value of the residuals for this fitting was 0.10 K.

Overall, the multiple Gaussian fitting of all of the resolved spectra returned a mean CO residuals rms of 0.24 K, while for ^{13}CO it was 0.15 K. These are virtually identical to the rms values of the portions of the spectra not showing line emission; hence the Gaussian fitting provides excellent line profile models. For the 14 C^{18}O lines, the mean residual rms was 0.063 K, and for the HCO$^+$ lines, the average was 0.029 K.

3.4.4 Analysis of the line profile fit results

The multiple Gaussian fitting created model line profiles which were excellent representations of nearly all the CO, ^{13}CO, C^{18}O, and HCO$^+$ spectra. This was not merely due the large number of fit parameters. Because the observed spectra are highly dispersed, the number of spectral channels with line emission greatly exceeded the number of fit parameters. For example, by specifying only six parameters, all 20 channels containing line emission for the ^{13}CO spectrum of Fig. 16 were well fit. This suggests that we may treat the model fit components as representing bona fide physical components of the gas velocity distribution along each line of sight. Thus, for the spectrum of Fig. 16, we identify the two fitted model Gaussians as delineating two distinct gas components along that direction, each possessing identifiable mean velocities and gas velocity dispersions.

For optically thin molecules, this process is straightforward. However, line transfer effects in the optically thick CO line make such interpretations riskier. As a partial justification for treating the analysis of the CO lines on an equal footing with that of the ^{13}CO lines, we point out that both species *independently* exhibit evidence of many of the same gas components, as described below. In what follows, we treat the fit results as representing legitimate, physical descriptions of the gas in LBN 11, and we proceed to determine the properties of the cloud components delineated by the Gaussian analysis.

For each molecule, all the fitted components were considered independent and histograms of the properties of the individual components were generated. Figure 17 shows multiple histograms of the fitted CO linewidths (FWHM), classified according to their fitted peak temperature. The bottom histogram shows how CO components with fitted peak temperatures below 1 K (T_A^*) are distributed in linewidth. Most were very narrow, displaying characteristic widths of about 0.2 km s^{-1}. However, some of the weak lines have widths greater than 0.5 km s^{-1}. For lines in the 1 to 2 K range, there were fewer narrow and wide lines, with most fitted widths lying between 0.2 and 0.6 km s^{-1}.

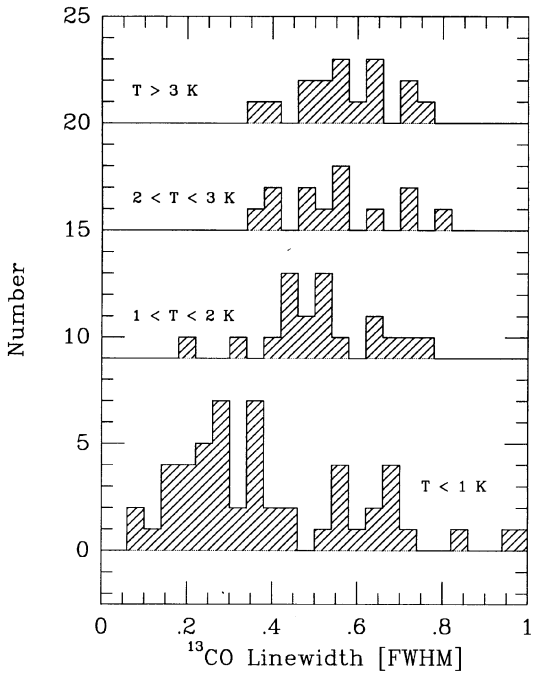

FIG. 18. Similar to Fig. 17, but for the ^{13}CO linewidth distributions, again separated into four intensity bins. Here the lines do not seem to broaden as much with increasing intensity as seen in the CO, indicating that the ^{13}CO lines are less saturation broadened.

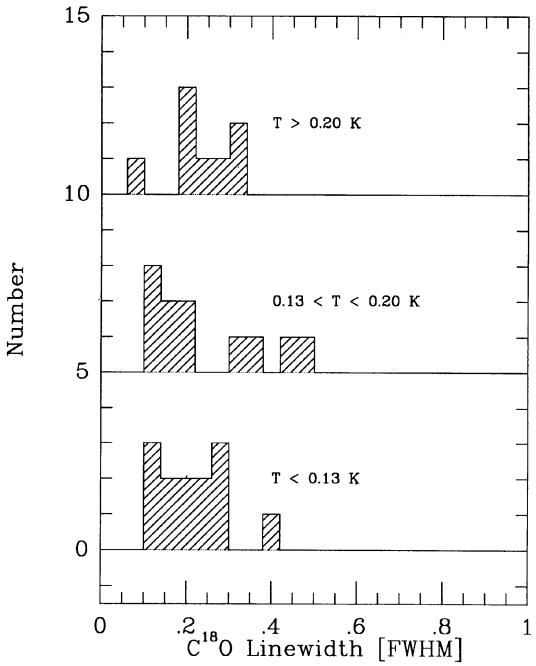

FIG. 19. Similar to Figs. 17 and 18, but for the C^{18}O linewidth distributions, for three intensity bins. Here, there is no change of linewidth with intensity, indicating that the lines are all optically thin. The linewidths found are clustered about means of 0.25 km s^{-1}, implying that the gas probed is very quiescent.

For the stronger lines in the two histograms at the top of the plot, the lines are characteristically wider, with a mean near 0.6 km s^{-1} for the strongest lines.

Figure 18 shows the analagous diagram for ^{13}CO. Here observations were made at fewer positions and there are fewer components, so the histograms are less well populated. Still, the faintest lines show a preponderance of narrow components, while the strongest lines have widths closer to 0.6 km s^{-1}. The C^{18}O diagram of linewidths, Fig. 19, shows very little variation of linewidth with line temperature. Instead, the C^{18}O components show mean widths of about 0.2–0.25 km s^{-1}. The C^{18}O is certainly optically thin and will reflect the extent of the true velocity field within the gas component it samples. The mean FWHM width for all C^{18}O components, weighted by the inverse square of the uncertainty in the widths, is 0.224 km s^{-1}. Following Dickman & Clemens (1983), the maximum turbulent velocity dispersion σ_0 (correcting for the thermal motion of the C^{18}O at 10 K) implied by this linewidth is 0.078 km s^{-1}. Hence, the ratio of turbulent-to-thermal motions in these components is around 30% (Mach number 0.30)—*these components contain only subsonic turbulence.*

An interpretation of Fig. 17, the distributions of CO linewidth, can be made on the basis of a simple saturation broadening model. As the CO becomes optically thick, if the intrinsic line shapes are narrow Gaussians with widths similar to those seen in the C^{18}O lines, the CO lines will broaden, developing flatter tops until self-absorption begins to split single components into two peaks. The shift of linewidth to larger values as the line temperature increases is the expected signature of saturation-broadened CO. Some of the weakest CO line components are probably misidentifications of a combination of spurious noise channels, non-Gaussian line edges or wings (although saturation broadened lines develop line edges which are sharper than unbroadened Gaussians), and extra components generated by self-absorptions. However, some of the weak CO lines may indicate the presence of gas components which are optically thin in the CO line.

Interpretation of the ^{13}CO lines within the optical depth broadening model is more problematic. The variation of width with line temperature is less dramatic in the ^{13}CO (Fig. 18) than in the CO. However, the mean ^{13}CO widths found for the stronger lines are almost as large as their CO counterparts. If the ^{13}CO lines are much less saturation-broadened than the CO lines, they ought to be narrower than the CO lines (see discussion in Dickman and Clemens). The ^{13}CO lines certainly have optical depths up to 2, but not the 100–200 expected of the CO. One partial resolution of this difficulty may be obtained by allowing the internal velocity field within each component to have a substantial systematic component (expansion, contraction, or rotation).

3.4.5 Rotation revisited—velocity coherence of Gaussian components

In the analysis of the rotation of the cloud presented in Sec. *3.3*, the velocities used to describe the gas along each sampled line of sight were the emission-weighted means. These had typical uncertainties of 80 m s^{-1}. However, the

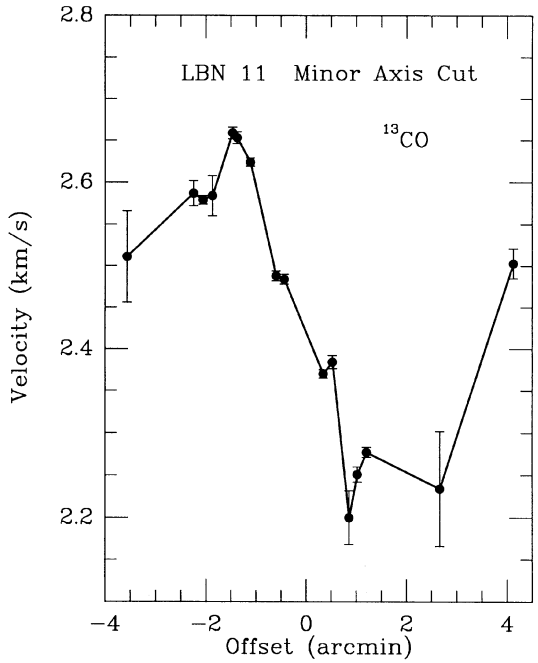

FIG. 20. Plot of the Gaussian fitted component velocities of ^{13}CO vs offset along the minor axis of the cloud. The physical rotation gradient across the central 4 arcmin is 5 km s^{-1} pc^{-1}. Outside the central 4 arcmin, the envelope is either not rotating, or weakly counter-rotating.

Gaussian component fitting analysis returned central velocity uncertainties closer to 20 m s^{-1} and often much less. If we provisionally accept their validity, these lower uncertainties allow us to probe the rotation of the cloud to a much finer level.

To do so, two cuts through the cloud were constructed, one along the previously identified rotation axis (the "major axis") and one perpendicular to that axis ("minor axis"). The cuts were chosen to pass through the refined cloud center at $(\Delta\alpha, \Delta\delta) = (1'.5, -1'.5)$. All of the fitted Gaussian components lying within 1.5 arcmin of each cut were included, with distance along the cut computed for each observed position. The component velocities were then plotted versus position along each cut.

The ^{13}CO components are particularly easy to interpret. Figure 20 shows the fitted velocites of the Gaussian components versus distance along the minor axis. The error bars reflect the fitted uncertainties. Components whose velocites were less than 2.1 or greater than 2.7 km s^{-1} were suppressed in the figure. (These are few, show much weaker line strengths than the ones used in Fig. 20, and do not seem to partake in the organized motion revealed in that figure.) Along the major axis, there is little organization, and no gradient indicative of rotation.

Along the minor axis, there is clearly a strong gradient in the inner 4 arcmin (0.13 pc), whose value is about 5 km s^{-1} pc^{-1}. This value should be compared to the value of 3.6 for the entire ^{13}CO region listed in Table 5, and to the value of 6.5 km s^{-1} pc^{-1} obtained from the core spectra analysis of Sec. *3.2*. Outside of the inner 4 arcmin, the velocity shift is either absent or perhaps even shows an opposite gradient. If taken at face value, this rotation curve strongly suggests that the core of LBN 11 is rapidly rotating. It also suggests a stationary or even counter-rotating envelope.

The fact that the Gaussian fit analysis revealed rotation in the core of LBN 11 of similar magnitude and direction as found in the coarser rotation analyses should be taken as partial verification of the authenticity of the line fitting technique. Also, counter-rotation in molecular clouds has been alleged before (Young *et al.* 1981) and studied theoretically (Mouschovias & Paleologou 1979; Gillis *et al.* 1979). Such differential rotation would reduce the magnitude of the rotational gradient found by global solid body fitting (Sec. *3.3*) below the values found from spatial–velocity probes, as in Fig. 20.

Direct analysis of the rotation curve under the assumption of simple Keplerian motion (i.e., ignoring the magnetic field) can be performed to indicate something about the distribution of mass in the core. The minor axis rotation curve was rectified and folded to yield an average rotation law for the core of LBN 11 traced by this collection of ^{13}CO components. Two results of the analysis are worth noting. First, the solid bodylike rise of the rotational velocity is direct evidence of a central hole in the mass distribution. Second, the decay of the rotation curve after the peak velocities are attained is very fast and implies an outer limit to the mass distribution of about 1–1.5 arcmin from the center. Thus the ^{13}CO-traced gas in this rapidly rotating component is distributed predominantly at a fixed distance of about 0.03 pc from the kinematic center of the cloud. The azimuthal distribution of the matter is probed via channel maps (Sec. *3.4.6*) and seems consistent with either two central clumps or a ring of gas, whose orbital plane is mostly parallel to the line of sight. Still under the Keplerian assumption, the total mass involved in the rapidly rotating ^{13}CO core is about 0.35 $\mathcal{M}_\odot$, which is similar to that found in the ^{13}CO clumps (see below), and in the CS and SO analysis (Sec. *3.2*).

3.4.6 Channel maps—feature catalogs

The next analysis was performed with the intention of spatially resolving the individual gas components. To do so, contour maps of emission toward LBN 11 for fixed velocity intervals (channels) were constructed from the CO and ^{13}CO spectra. The contour levels of the maps were selected to reflect steps of 2σ (0.5 K for CO and 0.3 K for ^{13}CO). Significant line emission spanned about 40 channels in the spectra; hence, that number of maps was created for each species. Figures 21 and 22 each display nine of the maps constructed for each molecule. The individual maps are presented on the same angular scale as the CO isotopic maps displayed earlier. Figure 21 shows the CO emission in channels centered at the velocities listed in the lower left corner of each panel. In the middle row of three panels, the velocities differ between neighboring panels by 0.195 km s^{-1}, or three channels. Significant differences in the spatial distribution of the emission can be seen. The ^{13}CO

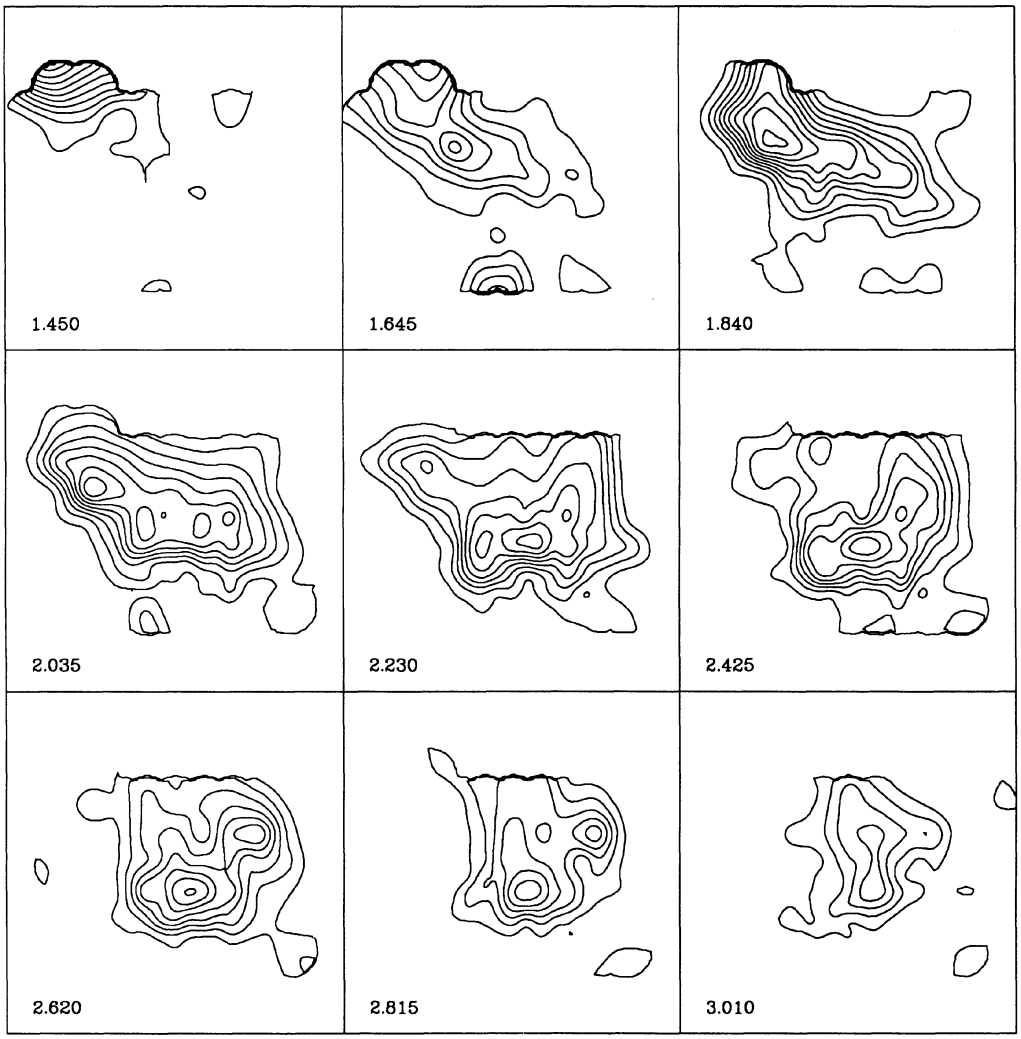

FIG. 21. Channel maps of the CO emission seen in nine of the spectral channels. The channel central velocity in km s^{-1} is indicated in the lower left corner of each map. The contours begin at 0.5 K and are stepped by the same amount.

channel maps in Fig. 22 were chosen to closely match the displayed CO maps in velocity (but unavoidably differ slightly, due to the different Doppler widths of the fixed frequency channels).

Self-absorption of the CO can be seen in these maps: in the centermost maps, the brightest ^{13}CO feature is almost perfectly placed between the two central CO features. Evidently, the CO suffers from absorption at this velocity in the direction of the peak ^{13}CO emission, leading to the depression of the CO contours and the bifurcation of the local CO emission into two apparent peaks. This position and velocity correspond to self-absorption region SA-1 (velocity 2.24 km s^{-1}) listed in Table 6.

Individual features were noted in each channel map and followed across neighboring maps to build a spatial and velocity profile for each resolved feature. A feature was deemed present in a map if it had two concentric contours (4σ) with at least 270° contour closure. Thus, for example, the centermost panel of Fig. 21 indicates the presence of four individual features. Moving three channels higher in velocity (right, center map) all four features are still present, but at different intensity levels, and at somewhat different locations. Once a feature was found on an individual channel map, the feature was characterized by its peak location, peak temperature, extents in major and minor axis directions, and the position angle of its major axis.

Features were followed in velocity (across different maps) until they could no longer be identified. The mean properties of each object were then computed by averaging the individual measurements made in each channel map containing the feature, weighted by the peak emission seen in the map times the area of the feature in the map. In this way, the properties are weighted by something approaching the velocity distribution of mass.

The cataloging of features on maps and linking of features across maps was performed separately on the CO and ^{13}CO channel maps. Tables 7 and 8 present summaries of the properties of the features found to exist across *more*

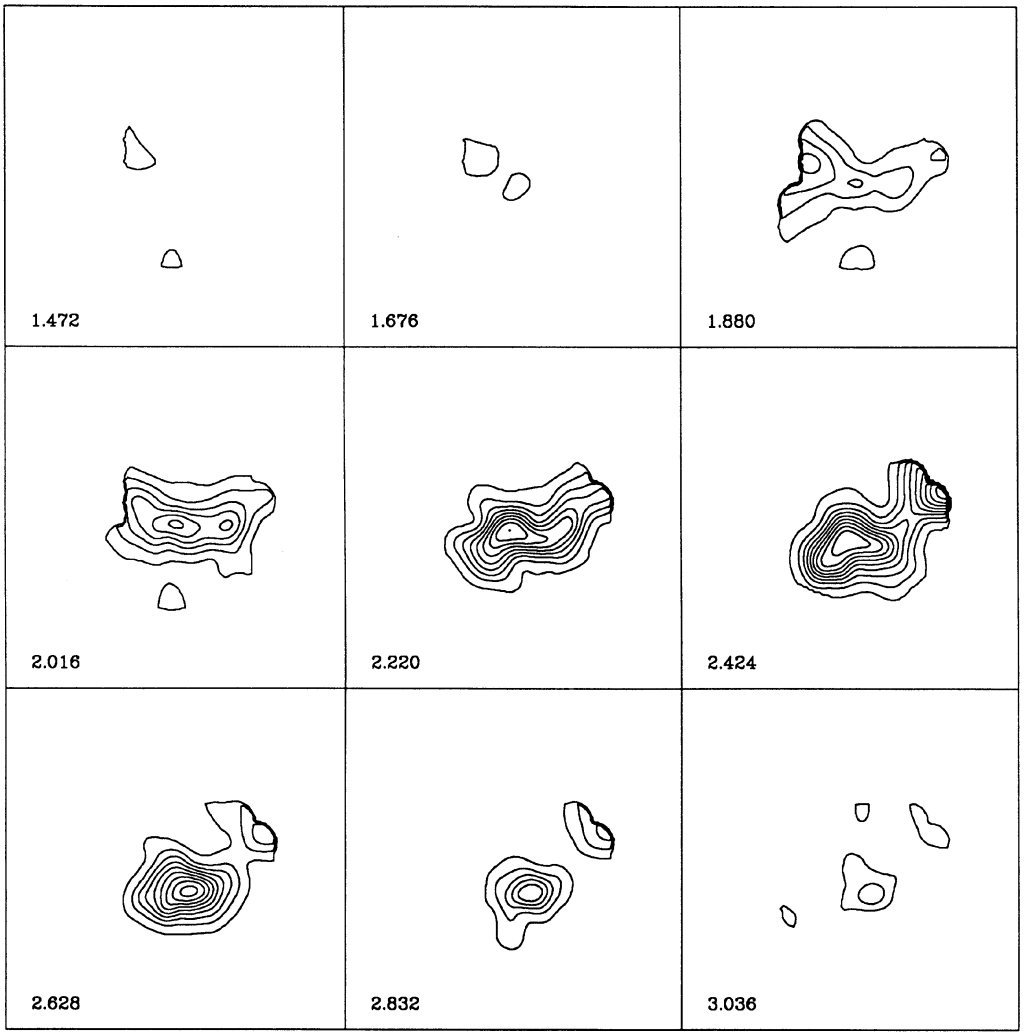

FIG. 22. Channel maps of the ^{13}CO emission seen in nine of the spectral channels. These maps differ from the CO maps in having significant emission over a smaller range of velocities and in having many fewer identifiable clumps of emission. The strong ^{13}CO rotation can be seen as a displacement of the location of emission southward as the velocity is increased.

than two consecutive channel maps. Since the features are mostly resolved spatially and are certainly resolved spectrally, it seems plausible to identify these features as independent gas features or "clumps" in the cloud. In the tables, the first column lists the R.A.-ordered clump identifying number. The second and third columns list the approximate centers of the clumps in relative offsets from the CO mapping center position. The fourth column lists the emission-weighted mean velocity for each clump, and the fifth column lists the similarly-weighted velocity dispersion about the mean velocity. The unweighted peak temperature of the clump is listed in column (6). Emission-weighted semimajor and semiminor extents and position angles are listed in columns (7) through (9). In the last column, labeled "Notes," we indicate if a clump is likely affected by self-absorption (for the CO), and whether there is a corresponding clump in the other table.

Three of the eleven CO clumps have ^{13}CO counterparts. All three of the ^{13}CO clumps have CO counterparts. The internal velocity dispersions of the clumps have means which are 50% of the thermal dispersions of hydrogen and helium gas at 10 K—we expect that these objects are the subsonic components found by the spectral line fitting. The cataloged clumps also do not account for all of the emission seen. There is a significant extended emission background in the CO maps; in the ^{13}CO maps a background is also present but is much fainter (see below).

The clump extents were used to compute mean diameters ($2\sqrt{ab}$) for each cataloged object. Figure 23 shows the resulting size histograms for the CO and ^{13}CO clumps. There seems to be a preferred size range for the clumps of about 0.1–0.2 pc, which is remarkably similar to the scale found in the magnetic field correlation analysis (0.1–0.2 pc, Fig. 3). The telescope beam size and resolution of the millimeter mapping grid steps set a lower cutoff of about

TABLE 7. Summary of CO clump properties.

Clump Number	Δ RA [arcmin]	Δ Dec [arcmin]	V_{LSR} [km s^{-1}]	σ_V [km s^{-1}]	T_A^* [K]	a [arcmin]	b [arcmin]	P.A. [°]	Notes
(1)	(2)	(3)	(4)	(5)	(6)	(7)	(8)	(9)	
CO–1	−3.1	1.9	2.65	0.161	3.2	2.46	1.86	+90	
CO–2	−1.9	0.3	2.20	0.164	3.5	3.79	2.49	0	C13 – 1, a
CO–3	0.1	−0.5	2.06	0.079	3.8	2.43	2.02	+18	
CO–4	0.8	−1.7	2.61	0.234	4.4	2.75	1.84	−86	C13 – 2, a
CO–5	1.2	1.9	2.95	0.124	2.3	3.12	2.04	+18	
CO–6	2.2	1.8	1.90	0.051	4.1	2.30	2.08	+90	
CO–7	3.8	−1.9	2.57	0.117	3.2	1.43	1.37	−11	a
CO–8	4.0	−0.4	2.08	0.058	3.8	2.76	2.14	0	
CO–9	4.1	−2.1	2.33	0.069	3.8	2.64	1.52	0	C13 – 3 (?), a
CO–10	7.2	2.4	1.87	0.150	5.6	4.55	2.28	+63	
CO–11	7.9	3.8	2.35	0.130	2.3	2.41	1.72	+46	

Notes:

a : Clump properties likely affected by spectral self-absorption (see text).

C13–n : Feature matches to ^{13}CO feature number n (see Table 8).

0.03–0.05 pc in our observations, so the peaks in the histograms are likely to be real.

The position angles of the major axes of the clumps show some degree of alignment with the direction of the local magnetic field. Figure 24 summarizes the histograms of angular differences between the position angles of the CO and ^{13}CO clumps and the direction of the local magnetic field, as traced by the optical polarization measurements. The horizontal axis is the acute angle between the major axis of each clump and the local magnetic field direction. In the lower panel of the figure, two cartoons indicate the relative clump–magnetic field alignment for the horizontal axis extremes. The histograms show that there is a tendency for the CO clumps to be oriented either parallel or perpendicular to the magnetic field direction, while the ^{13}CO clumps show a weak tendency for intermediate orientation. Perpendicular orientations (angle=90°) would be expected for gas clumps condensing along magnetic field lines.

No clumps were found to have significant rotation, although the technique for identifying clumps would tend to be insensitive to all but the most rapid rotation. A check for whether the individual clumps were participating in the general rotation of the cloud was also performed. The positions of the clump centers (from Tables 7 and 8) were used to predict the local cloud radial velocity, given the solid body rotation of the CO and ^{13}CO listed in Table 5. Differences between observed and predicted clump velocities were then computed. For the CO clumps, the mean difference was very small, 23 m s^{-1}, but the dispersion of the differences was 0.36 km s^{-1}. The ^{13}CO clumps showed about the same mean and dispersion seen in the CO clumps.

We interpret these results to imply that the individual

TABLE 8. Summary of ^{13}CO clump properties.

Clump Number	Δ RA [arcmin]	Δ Dec [arcmin]	V_{LSR} [km s^{-1}]	σ_V [km s^{-1}]	T_A^* [K]	a [arcmin]	b [arcmin]	P.A. [°]	Notes
(1)	(2)	(3)	(4)	(5)	(6)	(7)	(8)	(9)	
C13–1	−1.5	−0.5	2.10	0.136	2.9	2.67	1.72	−47	CO–2
C13–2	0.9	−2.2	2.72	0.163	3.1	2.30	1.39	−75	CO–4
C13–3	2.1	−1.0	2.26	0.204	3.3	2.57	1.65	−67	CO–9 (?)

Notes:

CO–n : Feature matches to CO feature number n (see Table 7).

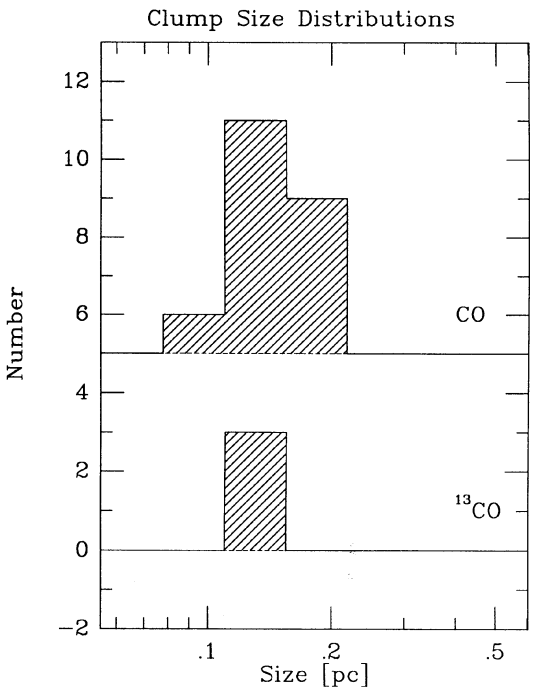

FIG. 23. Distributions of clump diameters of the CO and ^{13}CO clumps identified in the channel map analysis. This figure has the same horizontal axis as Fig. 3.

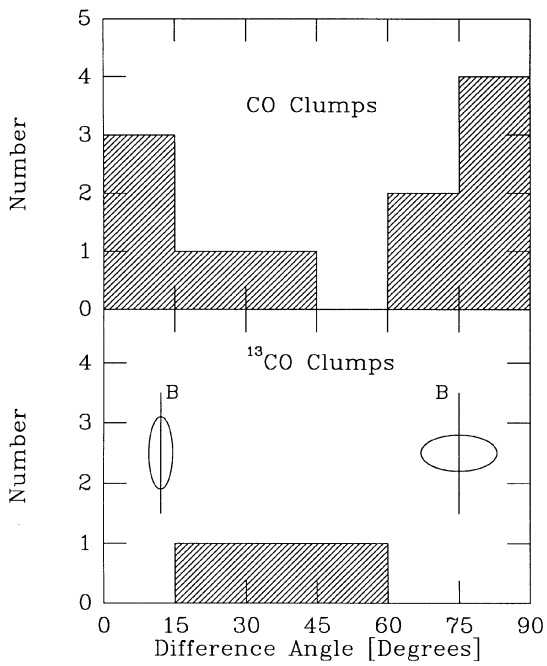

FIG. 24. Distributions of the differences between the clump elongation directions and the local magnetic field (mean stellar polarization) directions.

clumps are relatively quiescent, and that *as a population* they partake of the general cloud rotation. However, individual clumps are also likely to have transsonic orbital motions within the nonclump gas in LBN 11, if the nonclump gas is as cool as the clump gas. Additionally, there were two clumps (CO-1 and CO-5) which had very high velocities relative to the cloud rotation, in the range 0.4 to 0.8 km s^{-1}. It should be noted that although these velocities are transsonic they are not trans-Alfvènic (Alfvèn velocities are $\sim$0.5–0.6 km s^{-1} in the cool CO gas).

There are fewer clumps seen in ^{13}CO, and they are more centrally located than those seen in CO. The CO is much clumpier, and the clumps span a larger range of cloud locations and velocities. In this sense, CO is more strongly clumped than ^{13}CO. Earlier, we showed that ^{13}CO traced a higher cloud rotation rate than CO, and that the velocity extent of the ^{13}CO emission was smaller than that of the CO emission. Taken together, these findings can be reconciled by a picture of a cloud core delineated by ^{13}CO which is relatively detached from the ambient magnetic field, whose clumps are poorly aligned with the ambient magnetic field direction as a consequence. The surrounding cloud envelope, as traced by CO, is highly clumped, slowly rotating, and exhibits clump orientations which are well aligned with the strongly coupled ambient magnetic field.

In order to estimate the ratio of CO and ^{13}CO emission in identified clumps to the total molecular emission, the total emission for each clump was estimated. Each clump was assumed to be a two-dimensional Gaussian ellipse in the plane of the sky, and to have a Gaussian line profile. The relevant elliptical axes sizes and linewidths used were those tabulated in Tables 7 and 8. The total emission detected for each molecule was obtained from the integrated emission images represented in Figs. 5 and 7.

CO clumps were found to contain about 25% of the total CO integrated emission, while ^{13}CO clumps accounted for about 50% of the total integrated emission in that species. We infer that significant emission is likely present on both larger and smaller size scales than those of the identified CO and ^{13}CO clumps.

Individual clump masses were estimated in a similar fashion. We assumed that the roughly 2 $\mathcal{M}_\odot$ of gas traced by CO followed the clump emission fraction by having about 0.5 $\mathcal{M}_\odot$ (25%) residing in the CO clumps, and we apportioned this mass based on the relative integrated emission calculated for each clump. Similarly, the ^{13}CO-based mass of 1.48 $\mathcal{M}_\odot$ was assumed to have about 0.74 $\mathcal{M}_\odot$ in clumps. The range of clump masses found was 0.012 to 0.34 $\mathcal{M}_\odot$, with log-based means of 0.24 $\mathcal{M}_\odot$ for the ^{13}CO clumps and 0.03 $\mathcal{M}_\odot$ for the CO clumps.

In summary, the CO and ^{13}CO clumps found have masses around 0.03 to 0.2 $\mathcal{M}_\odot$, gas temperatures of 8–10 K, radii of about 0.08 pc, linewidths of about 0.2 km s^{-1}, and mean H_2 volume densities of roughly 250 cm^{-3} for the CO clumps and about 2000 cm^{-3} for the ^{13}CO clumps. The CO clumps are thus much smaller than the Jeans size for this density and are unlikely to be gravitationally bound objects. If they are density or velocity fluctuations in the cloud, their lifetimes will likely be of the order of their sizes divided by the sound speed of the gas, yielding about 0.3 million years, or their sizes divided by the Alfvèn speed,

yielding about 0.15 million years. For LBN 11, which we estimated to be older than a few million year (Sec. *3.3*), that implies that the CO clumps are transitory and recurring.

3.5 The Nature of the Clumps

The multiple components seen in the CO and ^{13}CO line profiles and the spatial localization of those components in the channel mapping analysis both indicate that the gas in LBN 11 is not distributed either uniformly or simply. However, the exact physical nature of the spectral and spatial features is not instantly obvious. These features could be bona fide regions of enhanced gas density, temperature, or molecular abundance. Or, they could represent coherence features in the line-of-sight velocity field, with no corresponding localized increase in gas density or other physical property. Such velocity coherence could represent a traveling or stationary wave phenomenon, generated with or without intervention of the magnetic field.

The gas "clumps" we have identified seem to fall into two categories: those in the lower density CO gas; and those in the high density gas in the cloud core. The lower density CO clumps are more numerous, seem mostly present in the cloud periphery, and have fewer ^{13}CO analogs. The higher density ^{13}CO clumps are fewer, are present in the core, and all have CO analogs, as well as CS, SO, and self-absorption analogs (see Sec. *3.6*, below).

We believe that the ^{13}CO clumps represent true density enhancements in the cloud core, and are not transitory phenomena: the strong variation of velocity with position in the ^{13}CO core, if due to unbound motion, should dissipate the core in a fraction of a crossing time. Instead, we interpret the core rotation and the ^{13}CO clump locations to indicate the presence of either a pair of dense clumps, a ring of dense gas, or a cylinder of dense gas. Theoretical studies of cloud collapse with rotation often find that similar structures quickly evolve into two blobs of self-gravitating gas (for example, see Boss 1986). This raises the possibility that we are witnessing the formation of a protobinary in LBN 11; if so, this would be the earliest such identification. Friction due to gas collisions or magnetic braking could remove angular momentum from the currently widely separated clumps, leading to the future formation of a closer, low mass binary star system.

The CO clumps, by contrast, do not appear to be significant density enhancements in the gas. Their somewhat errant velocites with respect to the locally rotating cloud gas seem to indicate that they may represent supersonic perturbations. However, simple supersonic gas motions should quickly damp out by shocking and heating the gas. The very uniform magnetic field in the periphery of the cloud may permit Alfvèn waves to be driven into the cloud envelope at velocites ($\sim$0.5–0.6 km s^{-1}) higher than the sound speed, even for modest magnetic field strengths (few μ Gauss). The possible correlation of the sizes of the CO clumps and the size scale of the magnetic field directional dispersion would then have a natural interpretation in terms of Alfvèn waves propagating through the cloud envelope.

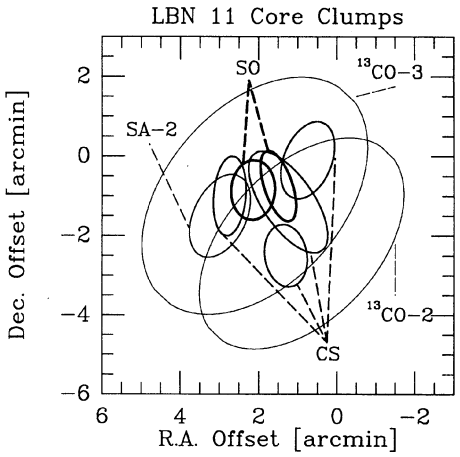

FIG. 25. Comparison of SO, CS, ^{13}CO emission regions and one region of CO self-absorption in the central region of LBN 11. Two ellipses drawn with thin lines indicate the approximate locations and extents of the two ^{13}CO clumps which overlap this region. The thickest lined ellipses indicate the locations and sizes of the SO emitting regions (see also Fig. 10). Thinner ellipses indicate the CS emitting regions and the CO self-absorbing region SA-2.

3.6 Future Star Formation Sites?

The distribution of the densest gas in the cloud, as traced by CS and SO, is shown in Fig. 25 in cartoon form. The ellipses depict the distributions, sizes, and orientations of the ^{13}CO clumps, SO and CS emitting regions, and one of the self-absorbed CO regions in the core of LBN 11. The visual impression is that the CS and SO and self-absorbed CO gas—that is, all the densest gas—is generally distributed *within* the ^{13}CO clumps, and along a line whose position angle is about $-60°$ (within 30° of the rotation axis). The locations of the CS and SO regions *at* the centers of the strongest ^{13}CO emitting regions confirms that the two are related, with the CS and SO tracing the densest gas contained in the ^{13}CO clumps. These are likely to be the sites of any current or future star formation in the globule.

4. SUMMARY

In order to investigate the relationship between embedded magnetic fields, cloud structure, and star formation, we have performed a multiwavelength study of the nearby small Bok globule LBN 11 (distance $\sim$110 pc, size $\sim$0.3 pc). Optical polarimetry of background stars was used to characterize and trace the embedded magnetic field direction. High-dispersion CO isotopic mapping was used to determine the radial density distribution of the gas, to measure cloud rotation, and to identify individual cloud gas clumps. CS and SO mapping revealed dense cores within the ^{13}CO clumps.

Analysis of co-added *IRAS* images reveal the cloud to be free of current or recent star formation: there are no infrared point sources of sufficient flux or proper colors to signify young stars associated with the cloud. Extended emission from the cloud was detected by *IRAS*, revealing a single central core region and dust temperatures at or below 21 K. The dust traced by *IRAS* is underluminous compared to the emission predicted for a similar-sized cloud embedded in the standard interstellar radiation field.

A magnetic field is clearly associated with the cloud, as revealed by the high levels of linear polarization exhibited by the sixteen background stars we observed. The magnetic field is unusually uniform, and possesses a directional dispersion ($<6°$) much smaller than that seen in any other molecular cloud studied to date. The field is parallel to the nearby Galactic magnetic field and almost parallel to the rotation axis of the cloud. The magnetic field of the cloud also exhibits a characteristic directional length scale ($\sim$0.1–0.2 pc).

The molecular line mapping data were analyzed to determine the mass, structure, and kinematics of the cloud. The mass is extremely low, about 2 $\mathcal{M}_\odot$. CO and ^{13}CO integrated intensity maps reveal a single cloud core region and a mean gas temperature of 9–10 K. The cloud exhibits bulk rotation in both the CO and ^{13}CO lines. The radial dependence of the gas density is similar to r^{-3}, with peak volume densities in the core of about 3×10^4 H_2 cm^{-3}. This value is similar to those returned from analyses of the CS and SO maps of the core region, indicating that there is no hidden dense gas missed by ^{13}CO probes. There are, however, some unresolved chemical abundance questions, one related to the exceedingly weak HCO^+ lines, another related to the dissimilar spatial distributions of CS and SO.

The molecular line maps show the cloud to be extremely clumpy. This condition is surprising, in view of the isolated, quiescent nature of the globule, and has not been seen previously in so small a cloud. Clumps were found to range in size from 0.2 pc for the largest CO clump to about 0.04 pc for the smallest CS feature. There appear to be two different populations of clumps. Those seen in the gas traced by CO are more numerous, tend to exist in the cloud envelope, have small individual masses ($\sim$0.02 $\mathcal{M}_\odot$), and seem to be unstable fluctuations. Clumps in the gas traced by ^{13}CO are fewer, exist in the cloud core region, have higher mean densities and masses, and are likely to be somewhat stable.

Detailed examination of the ^{13}CO rotation curve of the cloud shows evidence for strong differential rotation. The cloud core ($r<0.1$ pc) is rapidly rotating, perhaps in a Keplerian fashion produced by a young protobinary or ring of gas. Exterior to the core, the cloud envelope is either slowly rotating, or possibly counterrotating.

The size range of the CO and ^{13}CO clumps found (0.1–0.2 pc) is remarkably similar to the size range found for the maximum magnetic field directional dispersion. The CO clumps also exhibit some tendency to align along the magnetic field. We conclude that at least in the envelope of the cloud, the magnetic field and the CO clumps are coupled. However, in the core, our analysis of the gravitational, thermal, turbulent, magnetic, and rotational energies of the cloud do not allow for the presence of a magnetic field stronger than about 7 μG.

LBN 11 therefore appears to be a star-free, quiescent, differentially rotating, elongated, clumpy globule, possibly in the process of developing a protobinary in its core. A uniform magnetic field laces the cloud envelope, but may be slipping out of the cloud core, if not already absent there. In the envelope, the field is well-coupled to the gas, leading to correlated clump and magnetic field perturbation size scales. Since the gas clumps appear to be unstable, they may be a result of magnetic field effects, possibly Alfvén waves.

Santiago Tapia assisted in setting up Minipol and in some of the reductions. João Yun, Brian Kane, and Tom Skucas assisted in the November observing at FCRAO. Gaylin Laughlin and John Good of IPAC assisted in acquisition and interpretation of the co-added *IRAS* data. Nick Scoville was originally responsible for the SPECTRA spectral line analysis program, while Mike Brewer and Mark Heyer of FCRAO enhanced the porting and utility of the PC and UNIX versions used at BU. Partial funding for this project has included NASA (NAG 51160) and NSF (AST 8915606) grants and especially an NSF Supplemental Award under the Research Experiences for Undergraduates program (REU) (AST 9046651). The Five College Radio Astronomy Observatory is funded under NSF award AST 8815406 and is operated with permission of the Metropolitan District Commission of the Commonwealth of Massachusetts.

REFERENCES

Arons, J., & Max, C. E. 1975, ApJ, 196, L77
Arquilla, R., & Goldsmith, P. F. 1985, ApJ, 297, 436
Bally, J., & Langer, W. D. 1982, ApJ, 255, 143
Boss, A. P. 1986, ApJS, 62, 519
Clemens, D. P., & Barvainis, R. 1988, ApJS, 68, 257 (CB)
Clemens, D. P., & Tapia, S. 1990, PASP, 102, 179
Clemens, D. P., Yun, J. L., & Heyer, M. H. 1991, ApJS, 75, 877 (CYH)
de Geus, E. J., de Zeeuw, P. T., & Lub, J. 1989, AA, 216, 44
Dickman, R. L. 1978, ApJS, 37, 407
Dickman, R. L., & Clemens, D. P. 1983, ApJ, 271, 143
Dickman, R. L., McCutcheon, W. H., & Shuter, W. L. H. 1979, ApJ, 234, 100
Erickson, N. R., Goldsmith, P. F., Novak, G., Grosslein, R. M., Viscuso, P. J., Erickson, R. B., & Predmore, C. R. 1992, IEEE MTT 40, 1
Franco, G. A. P. 1989, A&A, 223, 313
Frecker, J. E., & Serkowski, K. 1976, ApOpt, 15, 605
Frerking, M. A., Langer, W. D., & Wilson, R. W. 1987, ApJ, 313, 320
Gillis, J., Mestel, L., & Paris, R. B. 1979, MNRAS, 187, 311
Goldsmith, P. F., & Arquilla, R. 1985, in Protostars and Planets II, edited by D. C. Black and M. S. Matthews (University of Arizona Press, Tucson), p. 137 (GA)

Goldsmith, P. F., Snell, R. L., Hemeon-Heyer, M., & Langer, W. D. 1984, ApJ, 286, 599
Hasegawa, T. I. 1987, Pub. Astr. Soc. Japan, 40, 219
Heyer, M. H. 1988, ApJ, 324, 311
Heyer, M. H., Vrba, F. J., Snell, R. L., Schloerb, F. P., Strom, S. E., Goldsmith, P. F., & Strom, K. M. 1987, ApJ, 321, 855
Hodapp, K.-W. 1987, ApJ, 319, 842
Irvine, W. M., Goldsmith, P. F., & Hjalmarson, Å. 1987, in Interstellar Processes, edited D. Hollenbach and H. Thronson, Jr. (Reidel, Dordrecht), p. 561.
Jones, T. J., Hyland, A. R., & Bailey, J. 1984, ApJ, 282, 675
Joshi, U. C., Kulkarni, P. V., Bhatt, H. C., Kulshrestha, A. K., & Deshpande, M. R. 1985, MNRAS, 215, 275
Kimura, T. & Tosa, M. 1991, MNRAS, 251, 664
Klebe, D., & Jones, T. J. 1990, AJ, 99, 638
Leung, C. M. 1985, in Protostars and Planets II, edited by D. Black and M. Mathews (University of Arizona Press, Tucson), p.104
Lynds, B. T. 1965, ApJS, 12, 163
Martin, R. N., & Barrett, A. H. 1978, ApJS, 36, 1
Mathewson, D. S., & Ford, V. L. 1970, MemRAS, 74, 139 (MF)
McCutcheon, W. H., Vrba, F. J., Dickman, R. L., & Clemens, D. P. 1986, ApJ, 309, 619
Mouschovias, T. Ch. 1976a, ApJ, 206, 753
Mouschovias, T. Ch. 1976b, ApJ, 207, 141
Mouschovias, T. Ch., & Paleologou, E. V. 1979, ApJ, 230, 204
Myers, P. C., & Goodman, A. A. 1988, ApJ, 329, 392
Myers, P. C., & Goodman, A. A. 1991, ApJ, 373, 509
Schneps, M. H., Ho, P. T. P., & Barrett, A. H. 1980, ApJ, 240, 84
Snell, R. L., Heyer, M. H., & Schloerb, F. P. 1989, ApJ, 337, 739
Swade, D. A. 1989, ApJ, 345, 828
Tapia, S. 1988, Preprints of Steward Observatory, No. 831
Turner, B. E., Xu, L., & Rickard, L. J. 1992, ApJ, 391, 158
Vrba, F. J., Luginbuhl, C. B., Strom, S. E., Strom, K. M., & Heyer, M. H. 1986, AJ, 92, 633
Vrba, F. J., Strom, S. E., & Strom, K. M. 1976, AJ, 81, 958
Vrba, F. J., Strom, S. E., & Strom, K. M. 1988, AJ, 96, 680
Williams, I. P., Vedi, K., Griffiths, W. K., Bhatt, H. C., Kulkarni, P. V., Ashok, N. M., & Wallis, R. E. 1985, MNRAS, 212, 181
Young, J. S., Langer, W. D., Goldsmith, P. F., & Wilson, R. W. 1981, ApJ, 251, L81
Yun, J. L., & Clemens, D. P. 1991, ApJ, 381, 474
Zealey, W. J., Ninkov, Z., Rice, E., Hartley, M., & Tritton, S. B. 1983, AstphlLet, 23, 119